A Triangular Discontinuous Galerkin Method for Non-Newtonian Implicit Constitutive Models of Rarefied and Microscale Gases

N. T. P. Le, H. Xiao, and R. S. Myong*

Department of Aerospace and System Engineering and Research Center for

Aircraft Parts Technology,

Gyeongsang National University, Jinju, Gyeongnam 660-701, South Korea

Abstract: The discontinuous Galerkin (DG) method has been popular as a numerical technique for solving the conservation laws of gas dynamics. In the present study, we develop an explicit modal DG scheme for multi-dimensional conservation laws on unstructured triangular meshes in conjunction with non-Newtonian implicit nonlinear coupled constitutive relations (NCCR). Special attention is given to how to treat the complex non-Newtonian type constitutive relations arising from the high degree of thermal nonequilibrium in multi-dimensional gas flows within the Galerkin framework. The Langmuir velocity slip and temperature jump conditions are also implemented into the two-dimensional DG scheme for high Knudsen number flows. As a canonical scalar case, Newtonian and non-Newtonian convection-diffusion Burgers equations are studied to develop the basic building blocks for the scheme. In order to verify and validate the scheme, we applied the scheme to a stiff problem of the shock wave structure for all Mach numbers and to the two-dimensional hypersonic rarefied and low-speed microscale gas flows past a circular cylinder. The computational results show that the NCCR model yields the solutions in better agreement with the direct simulation Monte Carlo (DSMC) data than the Newtonian linear

* Corresponding author: Tel: +82-55-772-1645.
Email: myong@gnu.ac.kr.

Navier-Stokes-Fourier (NSF) results in all cases of the problem studied.

Keywords: Discontinuous Galerkin, rarefied and microscale gas, nonlinear coupled constitutive relations

1 Introduction

In spite of considerable efforts over the past decades, an accurate numerical simulation of nonequilibrium rarefied and microscale gases remains very challenging in the field of computational fluid dynamics (CFD). Nonequilibrium gas flows of technological interest may be found in three distinctive problems [1-4]: 1) the hypersonic rarefied regime of trans-atmospheric vehicles; 2) the microscale low-speed (creeping) regime of micro- and nano-devices; and 3) the high-speed free-molecular regime of mechanical devices operating near the vacuum condition. The high Mach and Knudsen numbers are the sources of thermal nonequilibrium in these cases (the high Mach, the high Knudsen, or both). From past experiences, it was accepted that conventional models based on classical physics, such as the NSF equations, have serious limitations in capturing the correct flow physics of high thermal nonequilibrium. In the NSF equations, non-conserved variables associated with thermal nonequilibrium, the shear stress tensor and heat flux vector, are described in conjunction with the *linear uncoupled* constitutive relations of gradients of velocity and temperature. Note that these classical NSF relations are derived with the assumption that it is valid near local thermal equilibrium only. However, the near-local-thermal-equilibrium assumption is no longer applicable in rarefied and microscale gases because of the reduction of molecular collisions. Recently, in order to remove this shortcoming of the continuum approach, *nonlinear coupled* constitutive relations (NCCR) in a compact implicit algebraic form were derived [2,5,6] from the generalized hydrodynamic equations pioneered by Eu [7]. An important result obtained in those studies was that constitutive relations between stresses (heat flux) and the strain rate (the temperature gradient) are generally

nonlinear and coupled in states removed from thermal equilibrium. The new NCCR model has been successfully applied to some challenging problems of nonequilibrium gas flows where the NSF equations were found to be inappropriate.

In previous studies [2,5,6], the conservation laws with the non-Newtonian NCCR model were solved by applying the upwind type finite volume method (FVM) commonly used in the CFD community. In the course of these endeavors, however, it was recognized that the FVM is limited to second order accuracy at best, and in particular, it suffers a noticeable degradation in low Mach number flows. This deficiency is very critical because the NCCR model is envisioned to solve all three—the high Mach, the high Knudsen, and both—of regimes, including the high Knudsen and low Mach number regime, in a unified framework, which demands a capability to treat two extreme cases, high and low Mach number flows. This is the primary factor in the present study to employ the discontinuous Galerkin (DG) method, which demonstrated the ability to compute low Mach number flow problems, without resorting to the time-preconditioning techniques normally required for the FVMs.

The DG method has recently found its way into the main stream of CFD as an alternative approach for CFD based on the finite volume framework. This method combines key features of the finite element and finite volume methods, and has been successfully applied to a variety of problems, such as gas dynamics, acoustics, and magneto-hydrodynamics. It may be divided into modal [8-13] or nodal [14-18], depending on the basis function used in the scheme. The modal DG method had been developed for the one-dimensional (1D) Burgers equation [9,10,14], which is a simplified model equation of the conservation laws, and the two-dimensional (2D) compressible NSF equations [8,15,16,19]. An implicit nodal 1D DG scheme was also developed for the NSF equations to investigate the shock wave structure [15].

The essential idea of the DG method is derived from the fact that the shape functions can be

chosen so that either the field variable or its derivatives, or generally both, are considered discontinuous across the element boundaries, while the computational domain continuity is maintained. The calculations for higher dimensions require interpolation functions or shape functions defined in multi-dimensions. The extension of the 1D shape functions to multi-dimensional elements can be obtained using the tensor product approach [14]. Therefore, it can be effectively used in convection-dominant applications, while maintaining multi-dimensional geometric flexibility and higher local approximations through the use of higher order elements. This feature makes it uniquely useful for computational fluid dynamics and heat transfer [14,20]. In the DG method, field variables are considered discontinuous across elemental boundaries, circumventing the need of assembling a computationally demanding global matrix and leading to less in-core memory required in computation in comparison with the continuous Galerkin method. Moreover, this method can be easily parallelized due to its locality property and is thus well suited for parallel computer platforms [14]. This feature is particularly useful for computations in multi-dimensional domains because of the increase of the number of elements. These advantages, together with its ability to deal with high and low Mach number flows with a single framework, are the motivations for selecting the DG method for numerical solutions of the multi-dimensional conservation laws with the NCCR models in the present work. However, it should be mentioned that the DG method has a number of its own weaknesses. In particular, it involves high computational cost, memory requirement, and programming complexity in comparison with the FVM. In addition, it shows less tolerance to under-resolved solution features and requires high-order geometry representation.

There remains at present a critical computational issue regarding the application of the DG method to the conservation laws with the NCCR models. The essential feature of the DG method for the convection-diffusion type Newtonian linear NSF equations can be explained by considering the following viscous 1D Burgers equation:

$$\frac{\partial u}{\partial t}+\frac{\partial}{\partial x}\left(\frac{1}{2}u^2-\mu\frac{\partial u}{\partial x}\right)=0,\ \text{equivalently}\ \begin{cases}\dfrac{\partial u}{\partial t}+\dfrac{\partial}{\partial x}\left(\dfrac{1}{2}u^2+\Pi\right)=0,\\ \Pi=-S,\\ S=\mu\dfrac{\partial u}{\partial x}.\end{cases} \tag{1.1}$$

Likewise, the essential element of the new DG method suitable for the conservation laws with the non-Newtonian NCCR models can be illustrated by solving the following 1D NCCR-Burgers equation in *implicit* functional form [2]:

$$\begin{aligned}&\frac{\partial u}{\partial t}+\frac{\partial}{\partial x}\left(\frac{1}{2}u^2+\Pi\right)=0,\\ &\Pi=f^{-1}(-S)\ \text{ where }\ f(\Pi)=\frac{\sinh\Pi}{\Pi+1},\\ &S=\mu\frac{\partial u}{\partial x}.\end{aligned} \tag{1.2}$$

In passing, it should be mentioned that a similar non-Newtonian constitutive relation can be found in the viscoelastic flow [21]. The extension of the DG scheme initially developed for the simple Newtonian Burgers equation (1.1) to the more complicated non-Newtonian NCCR-Burgers equation (1.2) may seem straightforward, but there are two critical issues that require fundamental change of the scheme. First, the auxiliary variable S in the DG scheme of equation (1.2) should be $S = \mu u_x$, instead of $S = u_x$, which is commonly used in the DG scheme, since the viscosity μ is no longer constant, due to its temperature dependence, and thus depends on the primary variable u itself, and the constitutive relation in equation (1.2) is expressed in terms of μu_x. Second, the functional form of the constitutive relation in equation (1.2) is highly nonlinear and *implicit*, and requires an additional computational algorithm.

In this study, with special attention attached to these issues, we aim to develop an explicit modal DG scheme for solving multi-dimensional conservation laws in conjunction with the NCCR models. The main emphasis is placed on how to treat the complex non-Newtonian type

constitutive relations arising from the high degree of thermal nonequilibrium in multi-dimensional gas flow situation within the Galerkin framework. To the best knowledge of the authors, no *triangular modal DG method for non-Newtonian implicit constitutive models of hypersonic rarefied and low-speed microscale multi-dimensional gas flows* has been reported in the literature.

For the verification and validation study, we apply the scheme to the problems of the very stiff 1D shock wave structure for all Mach numbers [22-25] and the 2D hypersonic rarefied and low-speed microscale gas flows past a circular cylinder [26-30]. In particular, we consider the compressible low Mach number gas flow with high Knudsen number [26] in detail, one of most studied problem in microscale gas dynamics and yet remaining as extremely challenging from numerical viewpoint since the conventional NSF-FVM scheme and the DSMC suffer very poor accuracy and extraordinarily slow convergence.

The present paper is organized as follows. In Section 2 an explicit modal DG scheme with an auxiliary variable $\mathbf{S} = T^{S}\nabla\mathbf{U}$ is developed. The positivity preserving and slope limiters [13,31,32] and shock detection [10] are adopted for the present DG scheme for non-Newtonian constitutive models of rarefied and microscale multi-dimensional gas flows. The Langmuir velocity slip and temperature jump models [3,5,33,34], which are essential in any efficient computational simulation of rarefied microscale gas flows, are also implemented for the gas-surface molecular interaction in the DG framework. In Section 3 the DG scheme is extended to the multi-dimensional conservation laws with the NCCR models through two steps: first, considering a canonical scalar case (the 1D Newtonian and non-Newtonian Burgers equations) to develop the basic building blocks for the DG scheme, and second, application to the full system of multi-dimensional nonequilibrium gas dynamics. In Section 4 we present numerical results of the 1D shock wave structure problems, and the 2D hypersonic rarefied and microscale gas flows past a circular cylinder as the verification and validation of the new DG scheme. In addition, by

observing the degree of non-equilibrium and the nonlinear constitutive relations in gaseous expansion and compression cases, we explain the ultimate reason why the NCCR model always yields, in comparison with the NSF model, solutions that are in better agreement with DSMC results. In the last section we give the conclusions and discuss issues of further development in line of the present study.

2 Modal DG scheme with an auxiliary unknown $\mathbf{S}=T^{S}\nabla\mathbf{U}$

2.1 One dimensional NSF equations

The non-dimensional vector form of the conservation laws can be expressed as

$$\partial_t \mathbf{U}+\nabla\cdot\mathbf{F}_{\text{inv}}\left(\mathbf{U}\right)+\nabla\cdot\mathbf{F}_{\text{vis}}\left(\mathbf{U},\nabla\mathbf{U}\right)=0, \tag{2.1}$$

where variables in 1D case are defined as

$$\mathbf{U}=\begin{pmatrix}\rho\\ \rho u\\ \rho E\end{pmatrix},\quad \mathbf{F}_{\text{inv}}=\begin{pmatrix}\rho u\\ \rho u^2+\frac{1}{N_\delta \text{Re}}p\\ \left(\rho E+\frac{1}{N_\delta \text{Re}}p\right)u\end{pmatrix}\quad\text{and}\quad \mathbf{F}_{\text{vis}}=\frac{1}{\text{Re}}\begin{pmatrix}0\\ \Pi\\ \Pi u+\frac{1}{\text{Ec}\,\text{Pr}}Q\end{pmatrix}.$$

Here ρ is the mass density; u is the fluid velocity in the x-direction; p is the pressure; E is the total energy density; Π is the xx-component of the shear stress tensor, and Q is the x-component of the heat flux vector. The M, Re, N_δ, Ec and Pr are dimensionless gas dynamic parameters: Mach, Reynolds, composite, Eckert, and Prandtl numbers, respectively [2,5]:

$$M=\frac{u_r}{(\gamma RT_r)^{1/2}},\ \text{Re}=\frac{\rho_r u_r L}{\mu_r},\ N_\delta=\frac{\gamma M^2}{\text{Re}},\ \text{Ec}=(\gamma-1)M^2,\ \text{Pr}=\frac{C_{pr}\mu_r}{\kappa_r},$$

where the parameter γ is the specific heat ratio of gas, R is a gas constant, C_p denotes the heat capacity per mass at a constant pressure, and the subscript r represents the reference state. Also μ and κ are the viscosity and the thermal conductivity, respectively, expressed as

$$\mu = \kappa = T^s,$$

where s is a gas constant associated with the inverse power laws of gas molecules and T is the gas temperature. For the classical NSF model, the shear stress, Π, and the heat flux, Q, are computed as follows:

$$\Pi = -\frac{4}{3}\mu\frac{\partial u}{\partial x}, \quad Q = -\kappa\frac{\partial T}{\partial x}. \tag{2.2}$$

Finally the equation of state $T = p/\rho$ is used in the conservation laws.

2.1.1 One dimensional spatial discretization

The mixed DG formulation proposed in [8] is employed in spatial discretization of the NSF equations. This formulation will solve the second-order derivatives in viscous terms by adding auxiliary unknown **S**, because the second-order derivative cannot be accommodated directly in a weak formulation using a discontinuous function space. Therefore, **S** can be chosen to be the derivative of either primitive variables u, T or conservative variables **U**. In this work, **S** is chosen to be derivatives of the conserved variables **U,** that is, $\mathbf{S} = T^s\nabla\mathbf{U}$. This will result in a coupled system for **S** and **U**

$$\begin{cases} \partial_t\mathbf{U} + \nabla\cdot\mathbf{F}_{\text{inv}}(\mathbf{U}) + \nabla\cdot\mathbf{F}_{\text{vis}}(\mathbf{S},\mathbf{U}) = 0, \\ \mathbf{S} - T^s\nabla\mathbf{U} = 0. \end{cases} \tag{2.3}$$

The spatial derivatives of primitive variables such as u_x is then computed by expanding the derivatives of the conservable variables, for example $T^s u_x = (1/\rho)[T^s(\rho u)_x - T^s\rho_x u]$. Constitutive relations are given as $(\Pi, Q)_{\text{NSF}} = f_{\text{linear}}(\mathbf{S}(\mathbf{U}))$ for the NSF model, while they are given as $(\Pi, Q)_{\text{NCCR}} = f_{\text{non-linear}}(\mathbf{S}(\mathbf{U}), p, T)$ for the NCCR model. Notice that the introduction of an auxiliary variable such as one in (2.3) is necessary for the nonlinear *implicit* type NCCR constitutive model.

In order to discretize the coupled system (2.3), the numerical solutions of **U** and **S** are approximated by $\mathbf{U}_h$ and $\mathbf{S}_h$, respectively,

$$\mathbf{U}_h(x,t)=\sum_{i=0}^{k}U_j^i(t)\varphi^i(x),\quad \mathbf{S}_h(x,t)=\sum_{i=0}^{k}S_j^i(t)\varphi^i(x), \tag{2.4}$$

where φ is the basis function for finite element space and k is the order of approximation. It is assumed that the mesh covers the computational domain containing N elements (cells) I_j [$x_{j-1/2}$, $x_{j+1/2}$], for $1 \le j \le N$. The element is equally spaced $\Delta_x = x_{j+1/2} - x_{j-1/2}$ and the finite element space is defined as polynomials space:

$$V_h = V_h^k = \left\{\varphi \,|\, : \varphi|_{I_j} \in P^k(I_j),\ j = 1,\ldots,N\right\},$$

where $P^k(I_j)$ denotes the set of polynomials of degree up to k on the element I_j. The semi-discrete modal DG method for solving the coupled system (2.3) finds $\mathbf{U}_h$ and $\mathbf{S}_h \in V_h^k$. In this study, the orthogonal Legendre basis function is adopted for the function φ. It assumes that

$$\varphi^i(x) = P^i\left(\frac{2(x-x_j)}{\Delta x}\right),\quad 0 \le i \le k,\quad \xi = \frac{2(x-x_j)}{\Delta x},\quad -1 \le \xi \le 1,$$

where x_j is the center of the element. The first three orthogonal polynomials in [33] are used in this work, which correspond to the second-order approximation,

$$P^0(\xi) = \sqrt{0.5},\quad P^1(\xi) = \xi\sqrt{1.5},\quad P^2(\xi) = \left(1.5\xi^2 - 0.5\right)\sqrt{2.5}.$$

The coupled system (2.3) is multiplied with the basis function φ, and then integrated by parts for derivative terms over element I, the weak formulation of the coupled system can be derived to find $\mathbf{U}_h$ and $\mathbf{S}_h$

$$\begin{cases} \dfrac{\partial}{\partial t}\displaystyle\int_I \mathbf{U}\varphi dx - \int_I \nabla\varphi \mathbf{F}_{\text{inv}} dx + \int_{\partial I} \varphi \mathbf{F}_{\text{inv}} \cdot \mathbf{n} dx - \int_I \nabla\varphi \mathbf{F}_{\text{vis}} dx + \int_{\partial I} \varphi \mathbf{F}_{\text{vis}} \cdot \mathbf{n} dx = 0, \\ \displaystyle\int_I \mathbf{S}\varphi dx + \int_I T^s \nabla\varphi \mathbf{U} dx - \int_{\partial I} T^s \varphi \mathbf{U} \cdot \mathbf{n} dx = 0, \end{cases} \tag{2.5}$$

where ∂I denotes the boundaries of the element I and $\mathbf{n}$ is the outward unit normal vector. Equations of auxiliary unknowns are resolved first to compute the derivatives of conservative variables, in which the variable $T(x, t)$ is updated at each time step. The volume integrals within

the element *I* are resolved by the Gaussian quadrature with (*2k + 1*) Gaussian points to ensure accuracy [9]. The flux function $\mathbf{U}\cdot\mathbf{n}$, $\mathbf{F}_{\text{inv}}\cdot\mathbf{n}$ and $\mathbf{F}_{\text{vis}}\cdot\mathbf{n}$ in the boundary integrals of each element are replaced by a numerical flux function **h**, respectively.

2.1.2 One dimensional numerical fluxes

For the conservation laws there exist many numerical flux functions, such as Godunov, Roe, HLLE and Lax-Friedrichs. In the present study, the local Lax-Friedrichs (LxF) flux, $\mathbf{h}_{\text{inv}}$, is applied for inviscid terms. This is a monotone flux and is commonly used in the DG method. The LxF flux is the most dissipative flux that leads to a stable scheme in the DG framework. Note that the LxF flux is as dissipative as a stable explicit method can be for basic methods [36].

$$\begin{aligned}&\mathbf{F}_{inv}\cdot\mathbf{n}\approx\mathbf{h}_{\text{inv}}\left(\mathbf{U}^{-},\mathbf{U}^{+},\mathbf{n}\right)=\frac{1}{2}\left[\mathbf{F}_{\text{inv}}\left(\mathbf{U}^{-}\right)+\mathbf{F}_{\text{inv}}\left(\mathbf{U}^{+}\right)-C\left(\mathbf{U}^{+}-\mathbf{U}^{-}\right)\right]\\&\text{where}\quad C=\max\left(\left|u^{-}\right|+\frac{a_s^{-}}{M},\ \left|u^{+}\right|+\frac{a_s^{+}}{M}\right).\end{aligned}\tag{2.6}$$

Here $a_s = T^{1/2}$ is the speed of sound at an elemental interface. The signs – and + denote the left and right sides at an elemental interface. The term a_s/M instead of a_s appears in formulation of the coefficient *C* because of the definition of the characteristic speed in dimensionless form. For viscous terms, the central flux is applied to the remaining boundary integrals

$$\begin{aligned}&\mathbf{F}_{vis}\cdot\mathbf{n}\approx\mathbf{h}_{\text{vis}}\left(\mathbf{U}^{-},\mathbf{S}^{-},\mathbf{U}^{+},\mathbf{S}^{+},\mathbf{n}\right)=\frac{1}{2}\left[\mathbf{F}_{\text{vis}}\left(\mathbf{U}^{-},\mathbf{S}^{-}\right)+\mathbf{F}_{\text{vis}}\left(\mathbf{U}^{+},\mathbf{S}^{+}\right)\right],\\&\mathbf{U}\cdot\mathbf{n}\approx\mathbf{h}_{\text{aux}}\left(\mathbf{U}^{-},\mathbf{U}^{+},\mathbf{n}\right)=\frac{1}{2}\left[T^{s}\mathbf{U}^{-}+T^{s}\mathbf{U}^{+}\right].\end{aligned}\tag{2.7}$$

2.1.3 High order slope limiter and shock detection

The shock detection and high order slope limiter proposed in [10,32] are adopted for the present 1D DG scheme. The limiter is applied to eliminate oscillations in the shock simulations. The components of **U** can be limited as follows:

$$\tilde{U}_j^i=\min\text{mod}\left(U_j^i,U_{j+1}^{i-1}-U_j^{i-1},U_j^{i-1}-U_{j-1}^{i-1}\right),\quad i=1,\cdots,k,$$

with the minmod function

$$\min \mathrm{mod}\left(d_1, d_2, d_3\right)=\begin{cases}(\mathrm{sgn})\min\left(\left|d_1\right|,\left|d_2\right|,\left|d_3\right|\right) & \text{if } \mathrm{sgn}=\mathrm{sgn}\, d_1=\mathrm{sgn}\, d_2=\mathrm{sgn}\, d_3,\\ 0 & \text{otherwise.}\end{cases}$$

A shock detection proposed in [10] is also developed to identify the trouble cells (discontinuities) and to turn on the limiter to resolve the discontinuities. It is implemented into the DG scheme as follows:

$$D_j=\frac{\left|\int_{\partial I_j^-}\left(I_j-I_{nbj}\right)d\Gamma\right|}{\Delta x^{(k+1)/2}\left|\partial I_j^-\right|\left\|I_j\right\|},$$

where I_{nbj} indicates the neighboring element of I_j with a common boundary $\partial I_{j,nbj}$, and $||I_j||$ is the norm of I_j. The term ∂I_j^- locates at the point $x_{j-1/2}$, and the norm $\left|\partial I_j^-\right|$ drops out since it consists of only one point. The discontinuity detection scheme in [10] can be summarized as follows:

$$\begin{cases}\text{If } \ D_j>1\Rightarrow \mathbf{U}_h \text{ is discontinuous,}\\ \text{If } \ D_j<1\Rightarrow \mathbf{U}_h \text{ is smooth.}\end{cases}$$

2.1.4 Numerical boundary conditions

At the upstream boundary in 1D flow problem, all Euler characteristics are incoming for supersonic flow and therefore their initial values can be predetermined. Otherwise, at the subsonic downstream boundary, only one characteristic is incoming and thus one physical condition must be imposed [37]. In the present study of the shock wave structure, the downstream velocity specified by the Rankine-Hugoniot condition is retained to maintain the shock stationary. Other variables are extrapolated using the interior adjacent values. The computation at the downstream boundary cell I_N $[x_{N-1/2}, x_{N+1/2}]$ can be explained as follows:

$$
\begin{aligned}
&u_{N+1/2} = u_{\text{downstream},} \\
&\left(\rho u\right)_{N+1/2} = \rho_{N-1/2} u_{N+1/2}, \\
&p_{N+1/2} = \gamma M^2 \left(\gamma - 1\right)\left(\left(\rho E\right)_{N-1/2} - \frac{1}{2}\frac{\left(\rho u\right)^2_{N-1/2}}{\rho_{N+1/2}} \right), \\
&\left(\rho E\right)_{N+1/2} = \frac{p_{N+1/2}}{\gamma M^2 \left(\gamma - 1\right)} + \frac{1}{2}\frac{\left(\rho u\right)^2_{N+1/2}}{\rho_{N+1/2}}.
\end{aligned}
$$

Then the Dirichlet boundary condition is implemented at the downstream boundary $x_{N+1/2}$ by defining the exterior ghost states

$$
\frac{\mathbf{U}^+_{h,N+1/2} + \mathbf{U}^-_{h,N+1/2}}{2} = \mathbf{U}_{h,\text{downstream}},
$$

and the boundary condition for the $\mathbf{S}_h$ at the downstream boundary is set by

$$
\mathbf{S}^+_{h,N+1/2} = \mathbf{S}^-_{h,N+1/2}.
$$

A similar fashion of boundary conditions for $\mathbf{U}_h$ and $\mathbf{S}_h$ is also applied at the upstream boundary. Finally, the coupled system (2.3) can be obtained on each element

$$
\frac{\partial \mathbf{U}_h}{\partial t} = \mathbf{R}_h\left(\mathbf{U}_h\right), \tag{2.8}
$$

which is resolved by the Runge-Kutta time integration. The time step Δt is computed as [16]

$$
\Delta t = \frac{1}{(k+1)^2}\frac{\Delta x\, CFL}{|u| + \frac{a_s}{M} + \frac{\mu}{\Delta x}}, \tag{2.9}
$$

where *CFL* is the Courant-Friedrichs-Lewy condition ($CFL \le 1$).

2.2 Two dimensional NSF equations

We now extend the 1D DG scheme to develop a 2D DG scheme for multi-dimensional

conservation laws. The 2D NSF equations, in dimensionless form, are expressed as,

$$\partial_t \mathbf{U} + \nabla \cdot \mathbf{F}_{\text{inv}}(\mathbf{U}) + \nabla \cdot \mathbf{F}_{\text{vis}}(\mathbf{U}, \nabla \mathbf{U}) = 0,$$

with $\mathbf{F}_{\text{inv}} = (\mathbf{F}_{\text{inv1}}, \mathbf{F}_{\text{inv2}})$, where $\mathbf{F}_{\text{inv1}}$, $\mathbf{F}_{\text{inv2}}$ are the Cartesian components of inviscid terms, and $\mathbf{F}_{\text{vis}} = (\mathbf{F}_{\text{vis1}}, \mathbf{F}_{\text{vis2}})$, where $\mathbf{F}_{\text{vis1}}$, $\mathbf{F}_{\text{vis2}}$ are the Cartesian components of viscous terms.

$$\mathbf{U} = \begin{pmatrix} \rho \\ \rho u \\ \rho v \\ \rho E \end{pmatrix}, \quad \mathbf{F}_{\text{inv1}} = \begin{pmatrix} \rho u \\ \rho u^2 + \frac{1}{N_\delta \,\text{Re}}\, p \\ \rho uv \\ \left(\rho E + \frac{1}{N_\delta \,\text{Re}}\, p\right) u \end{pmatrix}, \quad \mathbf{F}_{\text{inv2}} = \begin{pmatrix} \rho v \\ \rho uv \\ \rho v^2 + \frac{1}{N_\delta \,\text{Re}}\, p \\ \left(\rho E + \frac{1}{N_\delta \,\text{Re}}\, p\right) v \end{pmatrix},$$

$$\mathbf{F}_{\text{vis1}} = \frac{1}{\text{Re}} \begin{pmatrix} 0 \\ \Pi_{xx} \\ \Pi_{xy} \\ \Pi_{xx} u + \Pi_{xy} v + \frac{1}{Ec\,\text{Pr}} Q_x \end{pmatrix}, \quad \mathbf{F}_{\text{vis2}} = \frac{1}{\text{Re}} \begin{pmatrix} 0 \\ \Pi_{xy} \\ \Pi_{yy} \\ \Pi_{yx} u + \Pi_{yy} v + \frac{1}{Ec\,\text{Pr}} Q_y \end{pmatrix},$$

where the stresses and heat fluxes are computed as

$$\Pi_{xx} = -\mu\left[\frac{4}{3}\frac{\partial u}{\partial x} - \frac{2}{3}\frac{\partial v}{\partial y}\right], \quad \Pi_{yy} = -\mu\left[\frac{4}{3}\frac{\partial v}{\partial y} - \frac{2}{3}\frac{\partial u}{\partial x}\right], \quad \Pi_{xy} = -\mu\left[\frac{\partial u}{\partial y} + \frac{\partial v}{\partial x}\right],$$
$$Q_x = -\kappa\frac{\partial T}{\partial x}, \quad Q_y = -\kappa\frac{\partial T}{\partial y}.$$

Here u and v are components of velocity in directions x and y, respectively, and the pressure p is computed by

$$p = \gamma M^2(\gamma - 1)\left(\rho E - \frac{1}{2}\rho(u^2 + v^2)\right).$$

2.2.1 Two dimensional spatial discretization

Using the same approach for 1D DG scheme, we obtain a similar coupled system in element I as in equation (2.3). The auxiliary variable $\mathbf{S}$ continues to be chosen as the derivative for

conservative variables $\mathbf{S} = T^{S}\nabla\mathbf{U}$. The spatial derivatives of primitive variables are also computed by expanding the derivatives of the conservable variables. Constitutive relations are defined as ($\mathbf{\Pi}$, $\mathbf{Q}$)$_{\mathrm{NSF}}$ = f_{linear}($\mathbf{S}$($\mathbf{U}$)) for the NSF model, while for the NCCR model they are given as ($\mathbf{\Pi}$, $\mathbf{Q}$)$_{\mathrm{NCCR}}$ = $f_{\mathrm{non\text{-}linear}}$($\mathbf{S}$($\mathbf{U}$), p, T). The numerical solutions of $\mathbf{U}$ and $\mathbf{S}$ are approximated by $\mathbf{U}_h$ and $\mathbf{S}_h$, respectively

$$\mathbf{U}_h(\mathbf{x},t) = \sum_{i=0}^{k} U_j^i(t)\varphi^i(\mathbf{x}), \quad \mathbf{S}_h(\mathbf{x},t) = \sum_{i=0}^{k} S_j^i(t)\varphi^i(\mathbf{x}), \quad \forall \mathbf{x} \in I, \tag{2.10}$$

where φ($\mathbf{x}$) is now the Dubiner basis functions for 2D solutions.

The choice of polynomial basis functions does not have much impact on the accuracy of the resulting scheme in the DG method. But an appropriate choice of basis functions may facilitate the implementation of the scheme. An important factor in using unstructured expansion for time-dependent calculations is the numerical efficiency of the algorithm in the context of cost per time step. Therefore, an unstructured expansion must be as numerically efficient as the structured expansion [38]. A suitable modal basis proposed by Dubiner for 2D problem [39] is adopted in the present work.

On the basis of a coordinate system for the unstructured expansions we construct a set of orthogonal polynomial expansions for unstructured grid system [38,39]. In the standard rectangular domain, the coordinates (a, b) are bound by constant limits, that is

$$\mathscr{R} = \{(a,b) \,|\, -1 \le a,b \le 1\}.$$

In order to develop a suitable basis for unstructured triangular regions described in Fig. 1, we need to develop a new coordinate system where the local coordinates have independent bounds. A suitable coordinate system, which describes the triangular region between constant independent limits, is defined by the inverse transformation [38,39],

$$r = \frac{(1+a)(1-b)}{2} - 1, \quad w = b.$$

New local coordinates (r, w) define the standard triangular region by

$$\mathcal{T} = \{(r,w) | -1 \le r, w;\ r + w \le 0\},$$

which is referred as the collapsed coordinate system shown in Fig. 1. The polynomial basis expansion $\{g_{lm}\}_{l,m \in \Omega}$ with $\Omega = \{l \ge 0,\ m \ge 0,\ l \le L,\ l + m \le W,\ L \le W\}$ are expressed as,

$$g_{lm}(a,b) = P_l^{0,0}(a)(1-b)^l P_m^{2l+1,0}(b), \tag{2.11}$$

where $P_n^{\varsigma,\eta}(x)$ is n^{th} order Jacobian polynomials [39]. For linear element P^1 polynomials approximation (W = 1), the orthogonal basis function φ can be expressed as

$$\{\varphi^i\}_{i=1}^3 = \{g_{00}, g_{01}, g_{10}\} \text{ or } \{g_{00}, g_{10}, g_{01}\}$$

and the basis functions in the present case are [16]

$$\begin{aligned} \varphi^1 &= 1, \\ \varphi^2 &= 1 + 2r + w = a(1-b), \\ \varphi^3 &= \frac{3w+1}{2} = \frac{3b+1}{2}. \end{aligned}$$

The coupled system (2.3) is multiplied with the basis function φ, and then integrated by parts for derivative terms over element I, the weak formulation of the coupled system in equation (2.3) is derived to find $\mathbf{U}_h$ and $\mathbf{S}_h$

$$\begin{cases} \dfrac{\partial}{\partial t}\displaystyle\int_I \mathbf{U}\varphi dV - \int_I \nabla\varphi \mathbf{F}_{\text{inv}} dV + \int_{\partial I} \varphi \mathbf{F}_{\text{inv}} \cdot \mathbf{n} d\Gamma - \int_I \nabla\varphi \mathbf{F}_{\text{vis}} dV + \int_{\partial I} \varphi \mathbf{F}_{\text{vis}} \cdot \mathbf{n} d\Gamma = 0, \\ \displaystyle\int_I \mathbf{S}\varphi dV + \int_I T^s \nabla\varphi \mathbf{U} dV - \int_{\partial I} T^s \varphi \mathbf{U} \cdot \mathbf{n} d\Gamma = 0, \end{cases} \tag{2.12}$$

where V and Γ denote volume and boundaries of the element I, respectively. Then, the essentially same treatment of auxiliary variables, volume integral, and boundary integral, which was developed for the 1D spatial discretization, is carried over to the 2D case.

2.2.2 Two dimensional numerical fluxes

Similar to 1D case, the LxF numerical flux is also adopted for computing directional fluxes of the inviscid terms,

$$\begin{aligned}
&\mathbf{F}_{\text{inv1}}\cdot\mathbf{nx}\approx\mathbf{h}_{\text{inv1}}\left(\mathbf{U}^{-},\mathbf{U}^{+},\mathbf{nx}\right)=\frac{1}{2}\left[\mathbf{F}_{\text{inv1}}\left(\mathbf{U}^{-}\right)+\mathbf{F}_{\text{inv1}}\left(\mathbf{U}^{+}\right)-C\left(\mathbf{U}^{+}-\mathbf{U}^{-}\right)_{\text{inv1}}\right],\\
&\mathbf{F}_{\text{inv2}}\cdot\mathbf{ny}\approx\mathbf{h}_{\text{inv2}}\left(\mathbf{U}^{-},\mathbf{U}^{+},\mathbf{ny}\right)=\frac{1}{2}\left[\mathbf{F}_{\text{inv2}}\left(\mathbf{U}^{-}\right)+\mathbf{F}_{\text{inv2}}\left(\mathbf{U}^{+}\right)-C\left(\mathbf{U}^{+}-\mathbf{U}^{-}\right)_{\text{inv2}}\right],\\
&C=\max\left(\left|\mathbf{u}^{-}\right|+\frac{a_s^{-}}{M},\ \left|\mathbf{u}^{+}\right|+\frac{a_s^{+}}{M}\right),
\end{aligned}\tag{2.13}$$

where **nx** and **ny** are outward normal vectors in direction *x* and *y*, respectively. The central flux is selected to calculate the numerical fluxes for solution of auxiliary variables and the viscous terms

$$\begin{aligned}
&\mathbf{F}_{\text{vis1}}\cdot\mathbf{nx}\approx\mathbf{h}_{\text{vis1}}\left(\mathbf{U}^{-},\mathbf{S}^{-},\mathbf{U}^{+},\mathbf{S}^{+},\mathbf{nx}\right)=\frac{1}{2}\left[\mathbf{F}_{\text{vis1}}\left(\mathbf{U}^{-},\mathbf{S}^{-}\right)+\mathbf{F}_{\text{vis1}}\left(\mathbf{U}^{+},\mathbf{S}^{+}\right)\right],\\
&\mathbf{F}_{\text{vis2}}\cdot\mathbf{ny}\approx\mathbf{h}_{\text{vis2}}\left(\mathbf{U}^{-},\mathbf{S}^{-},\mathbf{U}^{+},\mathbf{S}^{+},\mathbf{ny}\right)=\frac{1}{2}\left[\mathbf{F}_{\text{vis2}}\left(\mathbf{U}^{-},\mathbf{S}^{-}\right)+\mathbf{F}_{\text{vis2}}\left(\mathbf{U}^{+},\mathbf{S}^{+}\right)\right],\\
&\mathbf{U}\cdot\mathbf{n}\approx\mathbf{h}_{\text{aux}}\left(\mathbf{U}^{-},\mathbf{U}^{+},\mathbf{n}\right)=\frac{1}{2}\left[T^{s}\mathbf{U}^{-}+T^{s}\mathbf{U}^{+}\right].
\end{aligned}\tag{2.14}$$

Here the signs – and + denote the inside and outside of an elemental interface.

2.2.3 Extension of positivity preserving limiter to triangular element

In DG scheme numerical solutions may lead to negative density and pressure during the time marching. Therefore, the positivity preserving limiter is needed to enforce positive pressure and density at every element. By extending the work of Zhang and Shu [31] for quadrilateral elements in DG method, Kontzialis and Ekaterinar [13] developed a positivity preserving limiter for triangular elements based on the calculation at quadrature points. In the present study, we extend this positivity preserving limiter into 2D DG scheme according to our new approach, which is based on the calculation at three vertices and the centroid point of triangle. The limiting procedure contains two steps as follows:

The first step is to limit the density at every element. The density values at three vertices of

element, as shown in Fig. 2, are computed to determine the minimum density value, $\rho_{\min}$= min(ρ_1, ρ_2, ρ_3). The limited coefficient θ_1 is then evaluated as

$$\theta_1 = \min\left(\frac{\bar{\rho}-\omega}{\bar{\rho}-\rho_{\min}}, 1\right)$$

Where $\omega = \min(10^{-13}, \bar{\rho}, \bar{p})$ and $\bar{\rho}$, $\bar{p}$ are the mean density and pressure values of element, respectively. The high order components of the density variable are then limited by

$$\mathbf{U}(\mathbf{x},t) = U_j^0(t)\varphi^0(\mathbf{x}) + \theta_1 \sum_{i=1}^{k} U_j^i(t)\varphi^i(\mathbf{x}). \tag{2.15}$$

The second step is to limit the pressure at every element. To do so, all remaining conserved variables **U** must be limited at this step. The pressure values at three vertices of element are computed to determine the minimum pressure value $p_{\min}$ = min(p_1, p_2, p_3). If $p_{\min} < \omega$ then it is equal to find σ_1 ($0 \le \sigma_1 \le 1$) at the point * on the line C-1 to satisfy $p(x^*) = \omega$, as seen in Fig. 2,

$$x^* = \sigma_1 x_1^* + (1-\sigma_1)x_C^*, \tag{2.16}$$

where x_1^* is the coordinates at the vertex 1 and x_C^* is the coordinates at the centroid of element. Calculations are repeated for the lines C-2 and C-3 to find σ_2 and σ_3 and then, σ = min(σ_1, σ_2, σ_3) with $0 \le \sigma \le 1$, and the limited coefficient θ_2 = min(σ,1). The high order components of conservative variables are limited by

$$\mathbf{U}(\mathbf{x},t) = U_j^0(t)\varphi^0(\mathbf{x}) + \theta_2 \sum_{i=1}^{k} U_j^i(t)\varphi^i(\mathbf{x}). \tag{2.17}$$

2.2.4 Langmuir velocity slip and temperature jump boundary conditions

At this stage, it is necessary to introduce the velocity slip and temperature jump boundary conditions at the wall for the study of rarefied and microscale gases. Among various slip models, the Langmuir slip model based on the physical adsorption isotherm [33] is chosen in the present study for several reasons. First, it is mathematically simple, Dirichlet type rather than Neumann type, so that it is far easier to implement numerically. Second, the main interest in the present

study is to investigate the effect of the NCCR model relative to the NSF model, not the boundary wall effect. Lastly, the Langmuir model turned out to be qualitatively the same as the conventional Maxwell slip model in most cases [33]. The so-called Langmuir slip model was developed based on the Langmuir adsorption isotherm in [3,5,33,34], and was shown to yield good results for rarefied and microscale gas flows. This model takes the interfacial gas-surface molecular interaction into account. A coverage fraction, α ($0 \le \alpha \le 1$), of monatomic molecules reaching thermal equilibrium on the surface can be expressed, in dimensional form, as

$$\alpha = \frac{\beta p}{1+\beta p} \tag{2.18}$$

where p is the surface pressure and β depends on the surface wall temperature T_w and the interfacial interaction parameters. By considering the gas-surface molecular interaction process as a chemical reaction, the parameter β can be expressed [3,5,33,34],

$$\beta = \sqrt{\frac{\pi}{32}}\frac{\pi}{c^2}\frac{T_r}{T_w}\exp\left(\frac{D_e}{R_u T_w}\right)\frac{1}{p_r Kn}, \tag{2.19}$$

where c is gas constant of the exponent of the inverse power law for the particle interaction potential, p_r and T_r are reference pressure and temperature, R_u is universal gas constant, Kn is global Knudsen number defined as the ratio of the molecular mean free path λ and the characteristic length L, and D_e is the heat of adsorption; for example, D_e = 5,255 J/mol for Ar-Al molecular interaction model [33,34]. The velocity slip and temperature jump boundary conditions in the Langmuir model are determined according to the fraction, α,

$$\begin{aligned} \mathbf{u} &= \alpha \mathbf{u}_w + (1-\alpha)\mathbf{u}_g, \\ T &= \alpha T_w + (1-\alpha)T_g, \end{aligned} \tag{2.20}$$

where $\mathbf{u}$ is velocity vector, $\mathbf{u}_w$ is the wall velocity vector, $\mathbf{u}_g$ and T_g are gas velocity vector and temperature at reference location. All reference values are chosen from the far field conditions in the present work. The exterior ghost states are imposed to evaluate $\mathbf{U}^+$, $\mathbf{U}^-$, $\mathbf{S}^+$ and $\mathbf{S}^-$ at boundaries

as the 1D DG scheme. Finally, the system of 2D conservation laws can be obtained on each element

$$\frac{\partial \mathbf{U}_h}{\partial t} = \mathbf{R}_h\left(\mathbf{U}_h\right),$$

which is resolved by the fifth order Runge-Kutta time integration with Δt determined by equation (2.9).

3 Extension to the conservation laws with implicit NCCR

The conservation laws of gas flows (2.1) are still too complicated to study the DG method in detail. If a simplified model that contains the essence of the original convection-diffusion equations is derived, it can serve as a very useful guide. Such a model, called the Burgers equation, is already available, and it has been studied extensively in the field of wave propagation and turbulence [40]. In the present study, the following classical 1D Burgers equation (1.1) is first considered in order to develop the basic building blocks of an explicit modal DG scheme: in the usual convection-diffusion form,

$$\frac{\partial u}{\partial t} + u\frac{\partial u}{\partial x} = \mu\frac{\partial^2 u}{\partial^2 x}, \tag{3.1}$$

or, in the form of the conservation law and the constitutive relation,

$$\begin{aligned} &\frac{\partial u}{\partial t} + \frac{\partial}{\partial x}\left(\frac{u^2}{2} + \Pi_0\right) = 0, \\ &\Pi_0 = -S = -\mu u_x, \end{aligned} \tag{3.2}$$

with the exact solution

$$u\left(t,x\right) = u_r + \frac{u_l - u_r}{1+\exp\left[\left(u_l - u_r\right)\left(x - \bar{u}t\right)\right]/2\mu}, \quad \bar{u} = \frac{u_l + u_r}{2},$$

where u_l and u_r are the fixed boundary values, and $\bar{u}$ is the speed of shock and μ is the assumed constant. This equation will be designated as the *linear* 1D Burgers equation since the linear

constitutive relation is used in the scalar conservation law. The subscript 0 in Π_0 represents the linear constitutive relation. The numerical solutions of u and S are numerically approximated by $\boldsymbol{u}_h$ and $\boldsymbol{S}_h$ as in equation (2.4). The LxF flux is selected for solving the boundary integral of nonlinear term ($u^2/2$) with the coefficient C = max(u^-, u^+). The central flux is applied for the remaining boundary integrals to find $\boldsymbol{u}_h$ and $\boldsymbol{S}_h$ in weak formulation. The exterior ghost states are also defined to compute $\boldsymbol{u}_h$ and $\boldsymbol{S}_h$ at boundary conditions. The orthogonal Legendre basis functions presented above are used for calculations. The linear element and first-order Runge-Kutta time integration are applied to resolve ($\partial \boldsymbol{u}_h/\partial t$) = $R_h(\boldsymbol{u}_h)$. Elements are equally spaced in the computational domain.

On the other hand, the following 1D implicit NCCR-Burgers equation (1.2) is also implemented in the DG scheme:

$$\begin{aligned} &\frac{\partial u}{\partial t}+\frac{\partial}{\partial x}\left(\frac{u^2}{2}+\Pi\right)=0, \\ &\Pi q(\Pi)=(\Pi+1)\Pi_0, \text{ or } \Pi_0=\frac{\Pi q(\Pi)}{\Pi+1}, \text{ where } q(\Pi)=\frac{\sinh\Pi}{\Pi}, \\ &\Pi_0=-S=-\mu u_x. \end{aligned} \tag{3.3}$$

The values Π for a given known value of Π_0 are represented by the components S^i of $\boldsymbol{S}_h$ in the DG scheme. They are obtained by solving the nonlinear *implicit* algebraic equation (3.3) via the iterative method [2,5]: for positive and negative Π, respectively,

$$\Pi_{n+1}=\sinh^{-1}\left[\Pi_0\left(\Pi_n+1\right)\right], \text{ and } \Pi_{n+1}=\frac{\Pi_0}{q\left(\Pi_n\right)-\Pi_0}. \tag{3.4}$$

Solution of the iterative method for the 1D NCCR equation (3.3) is considered converged when

$$\left|\Pi_{n+1}-\Pi_n\right|\le 10^{-5}.$$

3.2 System of 1D conservation laws with implicit NCCR model

The following 1D NCCR model for the conservation laws developed on the basis of the moment method in [2, 5, 6] is implemented in 1D DG scheme:

$$\begin{pmatrix} \rho \\ \rho u \\ \rho E \end{pmatrix}_t + \begin{pmatrix} \rho u \\ \rho u^2 + \frac{1}{N_\delta \mathrm{Re}}\, p + \frac{1}{\mathrm{Re}}\Pi \\ \left(\rho E + \frac{1}{N_\delta \mathrm{Re}}\, p\right)u + \frac{1}{\mathrm{Re}}\Pi u + \frac{1}{\mathrm{Re}\, Ec\, \mathrm{Pr}} Q \end{pmatrix}_x = 0,$$

and

$$\begin{aligned} &\hat{\Pi} q(c\hat{R}) = (\hat{\Pi} + 1)\hat{\Pi}_0, \\ &\hat{Q} q(c\hat{R}) = (\hat{\Pi} + 1)\hat{Q}_0, \\ &\Pi_0 = -\frac{4}{3}\mu \frac{\partial u}{\partial x}, \quad Q_0 = -\kappa \frac{\partial T}{\partial x}, \end{aligned} \tag{3.5}$$

where the nonlinear factor $q(c\hat{R})$, describing the mode of energy dissipation accompanying the irreversible processes and the tenet of the modified moment method [7], is defined as

$$q(c\hat{R}) = \frac{\sinh(c\hat{R})}{c\hat{R}}, \quad \hat{R}^2 = \frac{3}{2}\hat{\Pi}^2 + \hat{Q}^2.$$

The ultimate origin of such factor lies with the consideration of entropy production and the cumulant expansion that provides a *resummation procedure* for an expansion in the Knudsen number series of the Boltzmann collision integral. Without such resummation procedure or similar procedure developed by Karlin *et al*. [41], which yields a non-Newtonian type explicit constitutive relation

$$\hat{\Pi} = \left(-3 + 2\hat{\Pi}_0 + 3\sqrt{1 - 4\hat{\Pi}_0 / 3 + 4\hat{\Pi}_0^2}\right) \Big/ \left(4\hat{\Pi}_0\right),$$

it will not be possible to derive such nonlinear factor. Such factor is also echoed in the well-known Eyring formula in non-Newtonian fluids [42], which describes shear thinning, i.e. the decrease of the viscosity with increasing the velocity gradient (or shear rate). Here gas constant c becomes $c = 1.0138$ for the Maxwellian monatomic gas molecule [43]. The caret ^ over a symbol

in the constitutive relations (3.5) represents the quantity with the following:

$$\frac{\Pi}{p},\ \frac{Q}{p\sqrt{C_p T/2\,\mathrm{Pr}}}.$$

It can be rewritten using the dimensionless parameters as follows:

$$\hat{\Pi} \equiv \frac{N_\delta}{p}\Pi,\ \ \hat{Q} \equiv \frac{N_\delta}{p}\frac{Q}{\sqrt{T/(2\varepsilon)}},\ \ \text{where}\ \ \varepsilon \equiv \frac{1}{\mathrm{Pr}\,\mathrm{Ec}T/\Delta T}.$$

The initial shear stress and heat flux in the NCCR model are computed by the values Π and Q at the elemental interfaces and the Gaussian points from the linear NSF model

$$\hat{\Pi}_0 \equiv \frac{N_\delta}{p} f_{\Pi\text{-linear}}\left(\mathbf{S}(\mathbf{U})\right),\ \ \hat{Q}_0 \equiv \frac{N_\delta}{p}\frac{1}{\sqrt{T/(2\varepsilon)}} f_{Q\text{-linear}}\left(\mathbf{S}(\mathbf{U})\right).$$

For positive and negative $\hat{\Pi}$ and $\hat{Q}$, the iterative procedures can be summarized as follows [2,3]:

$$\hat{R}_{n+1} = \frac{1}{c}\sinh^{-1}\left[c\left(\hat{\Pi}_n + 1\right)\hat{R}_0\right],\ \ \frac{\hat{Q}_{n+1}}{\hat{\Pi}_{n+1}} = \frac{\hat{Q}_n}{\hat{\Pi}_n} = \frac{\hat{Q}_0}{\hat{\Pi}_0}, \tag{3.6}$$

and

$$\hat{\Pi}_{n+1} = \frac{1}{q(c\hat{R}_n) - \hat{\Pi}_0}\hat{\Pi}_0,\ \hat{Q}_{n+1} = \frac{(\hat{\Pi}_n + 1)}{q(c\hat{R}_n)}\hat{Q}_0. \tag{3.7}$$

In these expressions, $\hat{\Pi}_1$ and $\hat{Q}_1$ are given by the equations

$$\hat{\Pi}_1 = \frac{\sinh^{-1}(c\hat{R}_0)\hat{\Pi}_0}{c\hat{R}_0},\ \ \hat{Q}_1 = \frac{\sinh^{-1}(c\hat{R}_0)\hat{Q}_0}{c\hat{R}_0}.$$

Solution of the iterative method for NCCR equations is considered converged when $\left|\hat{R}_{n+1} - \hat{R}_n\right| \le 10^{-5}$. The converged values at the iteration (n+1) are then embedded back into the DG scheme via the following relations:

$$\Pi = \frac{p}{N_\delta}\hat{\Pi}_{n+1}, \quad Q = \frac{p\sqrt{T/2\varepsilon}}{N_\delta}\hat{Q}_{n+1}.$$

3.3 System of 2D conservation laws with implicit NCCR model

In the case of 2D problem the stress and heat flux components (Π_{xx}, Π_{xy}, Q_x) on a line in the 2D physical plane induced by thermodynamic forces (u_x, v_x, T_x) can be approximated as the sum of two solvers: (1) one on (u_x, 0, T_x) and (2) another on (0, v_x, 0) [3,5]. From 1D NCCR, the equations for the first solver are given by

$$\hat{\Pi}_{xx} q(c\hat{R}) = (\hat{\Pi}_{xx} + 1)\hat{\Pi}_{xx_0},$$
$$\hat{\mathrm{Q}}_x q(c\hat{R}) = (\hat{\Pi}_{xx} + 1)\hat{\mathrm{Q}}_{x_0},$$

where

$$\hat{R}^2 = \frac{3}{2}\hat{\Pi}_{xx}^2 + \hat{\mathrm{Q}}_x^2.$$

The factor 3/2 in $\hat{R}^2$ originates from the symmetry relation

$$\hat{\Pi}_{yy} = \hat{\Pi}_{zz} = -\frac{1}{2}\hat{\Pi}_{xx}.$$

The equation for the second solver is given in the form

$$\hat{\Pi}_{xx} q^2(c\hat{R}) = -\frac{2}{3}(\hat{\Pi}_{xx} + 1)\hat{\Pi}_{xy_0}^2,$$

where

$$\hat{R}^2 = 3\hat{\Pi}_{xx}(\hat{\Pi}_{xx} - 1),$$

which follows from the symmetry relation

$$\hat{\Pi}_{xx} = \hat{\Pi}_{zz} = -\frac{1}{2}\hat{\Pi}_{yy},$$

and the constraint

$$\Pi_{xy} = \text{sign}(\Pi_{xy_0})\left[-\frac{3}{2}(\Pi_{xx}+1)\Pi_{xx}\right]^{1/2}. \tag{3.8}$$

The initial shear stresses and heat fluxes in 2D NCCR model are computed by the values Π_{xx}, Π_{xy} and Q_x at the Gaussian points in both volume and boundary integrals from the linear NSF model

$$\hat{\Pi}_{xx_0} \equiv \frac{N_\delta}{p} f_{\Pi_{xx}-\text{linear}}\left(\mathbf{S}(\mathbf{U})\right), \hat{\Pi}_{xy_0} \equiv \frac{N_\delta}{p} f_{\Pi_{xy}-\text{linear}}\left(\mathbf{S}(\mathbf{U})\right), \quad \hat{Q}_{x_0} \equiv \frac{N_\delta}{p}\frac{1}{\sqrt{T/(2\varepsilon)}} f_{Q_x-\text{linear}}\left(\mathbf{S}(\mathbf{U})\right).$$

These equations can be solved by the method of iteration that yields converged solution within a few iterations. The iteration procedures can be summarized as follows [3,5]. In the first solver (u_x, *0*, T_x) for positive $\hat{\Pi}_{xx}$ and $\hat{Q}_x$

$$\hat{R}_{n+1} = \frac{1}{c}\sinh^{-1}\left[c\left(\hat{\Pi}_{xx_n}+1\right)\hat{R}_0\right], \quad \frac{\hat{Q}_{x_{n+1}}}{\hat{\Pi}_{xx_{n+1}}} = \frac{\hat{Q}_{x_n}}{\hat{\Pi}_{xx_n}} = \frac{\hat{Q}_{x_0}}{\hat{\Pi}_{xx_0}},$$

for negative $\hat{\Pi}_{xx}$ and $\hat{Q}_x$

$$\hat{\Pi}_{xx_{n+1}} = \frac{\hat{\Pi}_{xx_0}}{q(c\hat{R}_n)-\hat{\Pi}_{xx_0}}, \; \hat{Q}_{x_{n+1}} = \frac{(\hat{\Pi}_{xx_n}+1)}{q(c\hat{R}_n)}\hat{Q}_{x_0}.$$

In these expressions $\hat{\Pi}_{xx_1}$ and $\hat{Q}_{x_1}$ are given by

$$\hat{\Pi}_{xx_1} = \frac{\sinh^{-1}(c\hat{R}_0)\hat{\Pi}_{xx_0}}{c\hat{R}_0}, \quad \hat{Q}_{x_1} = \frac{\sinh^{-1}(c\hat{R}_0)\hat{Q}_{x_0}}{c\hat{R}_0}.$$

In the solver on (0, v_x, 0) the $\hat{\Pi}_{xx}$ can be obtained for a given $\hat{\Pi}_{xy_0}$ through the equation

$$\hat{\Pi}_{xx_{n+1}} = -\frac{\hat{\Pi}_{xy_0}^2}{\frac{3}{2}q^2(c\hat{R}_n)+\hat{\Pi}_{xy_0}^2}.$$

and the $\hat{\Pi}_{xy}$ can be calculated by using the constraint (3.8). Solution of the iterative method for 2D NCCR equations is considered converged when $\left|\hat{R}_{n+1}-\hat{R}_n\right| \le 10^{-5}$. The converged values at the last iteration (n+1) are then implemented back into the 2D DG scheme as follows:

$$\Pi_{xx} = \frac{p}{N_\delta}\hat{\Pi}_{xx_{n+1}}, \quad \Pi_{xy} = \frac{p}{N_\delta}\hat{\Pi}_{xy_{n+1}}, \quad Q_x = \frac{p\sqrt{T/2\varepsilon}}{N_\delta}\hat{Q}_{x_{n+1}}.$$

4 Numerical results: verification, validation, and discussion

4.1 Scalar Burgers equation with linear and nonlinear constitutive relations: verification

As the first verification case, the shock structure profile of the 1D Burgers equation is computed by the 1D DG scheme. Fig. 3 shows the numerical results of the linear 1D Burgers equation at various values of the viscosity μ = 0.01, 0.1, 0.5 with N = 200, Δx = 0.05, and Δt = 0.0001 [14]. Initial values are set with u = 1 for x < 0 and u = –1 for x > 0. The values u = 1 and u = –1 are fixed at boundaries throughout the whole calculation. Steady state solution is reached when rms norm of u is below 10^{-8}. The 1D DG scheme of the linear 1D Burgers equation accurately predicts the profile in comparison with the exact analytic solutions. Figures 4 and 5 show the nonlinear effect of the 1D NCCR model in computational results for the cases μ = 0.1 and 0.5. Figure 6 also presents the normal stress Π profiles for the linear 1D Burgers and 1D NCCR-Burgers equations. The larger Π value in numerical solutions of the 1D NCCR-Burgers equation can be explained from a simple observation on the constitutive relations (3.2) and (3.3) that $\Pi_{NCCR} > \Pi_0$ when $0 < (-)\mu u_x < 3.4$, $\Pi_{NCCR} < \Pi_0$ when $3.4 < (-)\mu u_x$.

4.2 System of 1D conservation laws with NSF and NCCR: verification and validation

As a further verification and validation study of the 1D DG scheme, the celebrated hypersonic shock wave structure is considered. This problem has been a major stumbling block for theoreticians for a long time; for example, Grad [44] found that the shock structure solutions of his 13 moments equations break down completely, and from the theoretical phase portrait analysis of a dynamical system defined by ordinary differential equation of the shock structure, he proved that no solution exists for stronger shocks beyond the Mach number 1.65.

The shock wave structure problem considered here is defined as a very thin (order of mean free path; in other words, Knudsen number close to 1.0) stationary gas flow region between supersonic upstream and subsonic downstream. The upstream and downstream states, denoted by the subscripts 1 and 2, respectively, are determined by the so-called Rankine-Hugoniot condition:

$$\frac{\rho_2}{\rho_1}=\frac{u_1}{u_2}=\frac{(\gamma+1)M_1^2}{(\gamma-1)M_1^2+2},\ \ \frac{p_2}{p_1}=1+\frac{2\gamma}{\gamma+1}\left(M_1^2-1\right).$$

The stiffness of the shock wave structure due to the rapid change of physical properties in the thin region is the major cause of numerical difficulty in the problem. In this study, the upstream boundary values in the numerical calculation are set with $p_1 = u_1 = \rho_1 = T_1 = 1$ at the initial condition and are maintained throughout the whole computational procedure. A computational domain 60λ is used in all cases, covering the entire shock structure. The Maxwellian monatomic gas with $s = 1.0$, $c = 1.0138$, Pr = 0.75, $CFL = 0.5$, and $\Delta x = 0.2$ are used for simulations. A steady state solution is reached when the rms norm of the density is below 10^{-9}. The linear element (P1) with the first-order Runge-Kutta method (RK1) and the quadratic element (P2) with the second-order Runge-Kutta method (RK2) are tested for the case $M = 5$. As shown in Fig. 7, the numerical results are found indistinguishable, so the scheme with the linear element and the first-order Runge-Kutta method are selected for all remaining shock structure calculations. The results are normalized with respect to the upstream value; for example, in case of the density profile,

$$\bar{\rho}=\frac{\rho-\rho_1}{\rho_2-\rho_1}.$$

The central position $x = 0$ is defined as the location where the local density becomes equal to the arithmetic average of the upstream and downstream density. In the plots we use x/λ, where the mean free path is $\lambda=\mu/(\pi/2RT)^{1/2}/\rho$, as space variable.

The numerical solutions of shock structures are also compared with a full analytical NSF solution of dimensionless density r in closed elementary functional form in case of Pr=3/4 and Maxwellian molecule, which was recently derived by Myong [45],

$$3\theta_1 M\sqrt{\frac{\gamma\pi}{2}}\frac{x}{\lambda}=\frac{1}{r_a}\left(\frac{5}{4}+\frac{1}{2r_a}\right)-\frac{1}{r}\left(\frac{5}{4}+\frac{1}{2r}\right)+\frac{4}{\chi}\ln\frac{\left[(r_1^{-1}-r^{-1})/(r_1^{-1}-r_a^{-1})\right]^{(2\zeta-r_1^{-2})/r_1}}{\left[(r^{-1}-r_2^{-1})/(r_a^{-1}-r_2^{-1})\right]^{(2\zeta-r_2^{-2})/r_2}},$$

where

$$r_{1,2}=\frac{1}{v_{1,2}}=\frac{8}{5\pm\chi},\ r_a=\frac{1}{2}(r_1+r_2)=\frac{5}{4\zeta},\ \theta_1=\frac{15-2\chi-\chi^2}{64},$$
$$\chi=\sqrt{25-32\zeta},\ \zeta=\frac{\gamma^2M^2\left[2+(\gamma-1)M^2\right]}{2(\gamma-1)(1+\gamma M^2)^2}.$$

Here the upper sign is for the upstream 1 and the lower sign is for the downstream 2. Numerical solutions of the 1D DG and 1D FVM schemes for the NSF and NCCR models are compared in Figs. 8-11. For the NSF model, the numerical results agree well with the exact analytical solutions, even in very stiff Maxwellian molecule case with high Mach number 15. The DG NCCR results also show good agreement with the FVM NCCR results obtained in previous studies [2,5]. The difference between the numerical results of the NSF and NCCR models in Figs. 9 and 11 is due to the nonlinearity of the NCCR model. This nonlinearity in the constitutive relation is best illustrated in Fig. 12 of the numerical results of heat fluxes and shear stresses. There is a noticeable difference in the trajectories of the NSF and NCCR results in the phase diagram of shear stress and heat flux. For completeness, the normalized density profiles at various Mach numbers (M = 1.5, 10, and 12) for the NCCR model are presented in Fig. 13. Finally, as a validation study of shock structure, the inverse of the shock density thickness with the NSF and NCCR models is shown in Fig. 14. The inverse of the shock density thickness δ is defined as

$$\frac{1}{\delta} = \frac{\max\left(\frac{\partial \rho}{\partial x}\right)}{\rho_2 - \rho_1}.$$

This quantity, among others such as the shock asymmetry and the density-temperature separation distance [45], has been considered the primary parameter to characterize the shock structure profile. The computational results show good agreement between the exact analytic solution and DG results for the NSF model. Moreover, it can be observed that the results of the NCCR model are smaller than the solutions of the NSF model, which may be considered an important outcome to support the validity of the NCCR computational model. Indeed, it can be confirmed from Figs. 15 and 16 of monatomic gases that the NCCR results are in better agreement with the Burnett and DSMC data [46] and experimental data [22-24] than the NSF results.

4.3 System of 2D conservation laws with NSF and NCCR: verification and validation

In this subsection, 2D DG scheme is validated for viscous compressible gas flows past a circular cylinder for both hypersonic rarefied [28] and low speed microscale [26] flows. The input parameters and far field values denoted by the subscript, ∞, for hypersonic cases are M_∞ = 5.48, p_∞ = 5Pa, T_∞ = 26.6K, T_w = 293.15K, *CFL* = 0.1, and radii of the cylinders R = 1.9mm, 0.19mm corresponding to Kn = 0.05, Kn = 0.5, respectively. In the microscale case those values are M_∞ = 0.1, p_∞ = 101,325Pa, $T_\infty = T_w$ = 273K, *CFL* = 1.0 and the cylinder radius R = 0.313μm, yielding Kn = 0.1. Working gas is assumed argon for both cases with Pr = 2/3, c = 1.0179 and s = 0.75 for all 2D cases. The typical triangular meshes are depicted in Fig. 17 and the outer radius of the computational domain is chosen $R_{\text{outer}} = 30R$. The computational domain is defined by unstructured meshes with 120×60 in which 120 and 60 points are placed in circumferential and radial directions of the cylinder, respectively. The Langmuir slip and jump boundary conditions are applied at the solid surface and the far field boundary condition is imposed on the outer boundary of computational domain. The results of both the NSF and NCCR models are compared

with DSMC data generated by the sophisticated DSMC code [47] with full tangential momentum and thermal accommodation coefficients for slip and jump boundary conditions for all cases. Even though the linear element (P1) and the quadratic element (P2) are tested for 2D cases, the numerical results of the linear element only are presented since both results turn out to be indistinguishable.

4.3.1 Hypersonic rarefied case: M = 5.48 *and* Kn = 0.05, 0.5

The normalized densities and temperatures predicted by DG (NSF, NCCR) and DSMC methods along the stagnation streamline are compared in Figs. 18 and 19 for the hypersonic rarefied case, M = 5.48, Kn = 0.05. A comparison with another similar model—gas kinetic scheme result of nonlinear model Boltzmann equations by Yang and Huang [27]—for the cylinder flow case is presented in Fig. 18. The flow consists of a compressive bow shock structure, a stagnation region near the frontal part of the cylinder, and a gaseous expansion region near the rear part of the cylinder. The density and temperature remain initially constant at the free-stream region and then experience a rapid change of flow properties across the bow shock very close to the value given by the Rankine-Hugoniot relations in all methods. There is, however, significant discrepancy in the location and inner profiles of the bow shock between the near-local-equilibrium NSF solutions and the far-from-equilibrium NCCR/DSMC solutions. Notice that the new NCCR model yields density and temperature profiles in better agreement with DSMC data than the conventional NSF model. Also, as shown in Fig. 20, the normalized slip velocities increase gradually for the angle, θ, from $0^o \le \theta \le 130^o$ and reach peak normalized values around the location $\theta = 130^o$ (0.426 for the NSF model, 0.390 for the NCCR model, and 0.366 for DSMC). After reaching these normalized peak values, slip velocities decrease quickly to zero value at $\theta = 180^o$. Again, the NCCR model is shown in better agreement with DSMC data of velocity slip than the NSF model.

For completeness, detailed comparisons of normalized density contours of two hypersonic rarefied cases Kn = 0.05 and Kn = 0.5 are presented in Figs. 21 and 22, respectively. The results of the case Kn = 0.05 show that the density contours and the stand-off shock structure predicted by the NCCR model and the DSMC, as seen in Fig. 21, are in almost perfect agreement. At the same time, it can be noted that non-negligible discrepancies already begin to show up in case of the NSF model. In order to highlight the difference between the NSF and NCCR models, an additional higher Knudsen number case, Kn = 0.5, is considered. Figure 20 clearly shows that the normalized density field and the stand-off shock structure predicted by the NCCR model remain very close to those of DSMC data even in this high transitional regime, while those of the NSF model are in significant disagreement. The thickness of stand-off shock structure predicted by the NSF model is much smaller than that of the NCCR model and DSMC, as seen in Fig. 22. In addition, the degree of gaseous expansion near the rear part of the cylinder predicted by the NSF model is considerably higher than that of the NCCR model and DSMC. On the whole, the results of the non-Newtonian NCCR model show better agreement with DSMC data than the Newtonian NSF results in hypersonic rarefied cases studied.

4.3.2 Low-speed microscale case: M = 0.1 *and* Kn = 0.1

As mentioned in the Introduction, the compressible low Mach and high Knudsen number gas flow occupies a special place in numerical studies of rarefied and microscale gases, since the conventional FVM scheme and the DSMC suffer very poor accuracy and extremely slow convergence. In fact, this low-speed microscale case provides a rare instance that the NCCR model can not only handle the high Knudsen number flow in high transitional regime, but can also outperform the DSMC in aspect of quality of solutions obtained.

The normalized slip velocities predicted by NSF, NCCR, and DSMC methods on the solid surface of the cylinder are compared in Fig. 23 for the low-speed microscale case, M = 0.1, Kn =

0.1. The flow consists of smooth compression and stagnation regions near the frontal part of the cylinder, and a modest expansion region near the rear part of the cylinder. The NSF and NCCR normalized slip velocities rise gradually until the location $\theta = 130^o$ and reach peak normalized values: 0.0975 for the NSF model, and 0.1188 for the NCCR model. Past these peak values, the NSF and NCCR slip velocities decrease quickly to zero value at $\theta = 180^o$. The DSMC slip velocity increases gradually in the region $0^o \leq \theta \leq 110^o$ and thereafter decreases to zero value at $\theta = 180^o$. However, there exist significant uncertainties, as high as 45 percent, in case of DSMC slip velocity data caused mainly by low Mach number, casting serious doubt on any definite conclusions that might be drawn from them. This problem of poor performance in the DSMC method is well documented in literature [26]; indeed, this is exactly the reason why the high order continuum based method like the NCCR model is required to solve the compressible low Mach and high Knudsen number gas flow.

Nonetheless, some instructive results can still be drawn when the normalized density contours as presented in Fig. 24, instead of slip velocities, are examined. It can be noticed that the DSMC data produce relatively smooth contours near the cylinder and thus the direct comparison with the NSF and NCCR results becomes meaningful. The figure shows that (1) the NCCR results are more close to DSMC data; for example, the location and shape of density contour with $\rho = \rho_\infty$; (2) similar to the hypersonic case, the degree of gaseous expansion near the rear part of the cylinder predicted by the NSF model is considerably higher than that of the NCCR model and DSMC. Overall, the non-Newtonian NCCR model yields uncertainty-free results in better agreement with the DSMC data than the Newtonian NSF model.

4.4 Discussion

Numerical computations of the flow problems studied so far indicated that the computing time of the two-dimensional DG-NCCR code is comparable to that of the DG-NSF code. The only

excess load, which is caused by the addition of few iterations (less than 10 in most cases) when the stress and heat flux are calculated from the implicit algebraic constitutive equations for given thermodynamic forces, occupies a small fraction of computing time in the code (about 30 percent).

Finally, it is worthwhile discussing a reason behind the better performance of the new NCCR model over the conventional NSF model in deeper level. In Fig. 25 (a), the contours of velocity magnitude and several representative streamlines in high transitional regime are shown in order to provide detailed information of what gas particles experience–for example, acceleration or deceleration–and of how the NSF and NCCR models describe them differently. In addition, in Fig. 25 (b), the contours of the degree of thermal nonequilibrium [2], $\hat{R}$, which was derived from the Rayleigh-Onsager dissipation function [7], are shown in order to identify what regions are expected to deviate significantly from near-local-equilibrium assumption:

$$\hat{R} = N_\delta \left(\mathbf{\Pi} : \mathbf{\Pi} + \frac{2\varepsilon}{T} \mathbf{Q} \cdot \mathbf{Q} \right)^{1/2} \Big/ p \qquad \text{where}$$

$$N_\delta = \sqrt{\frac{2\gamma}{\pi}} M\text{Kn}, \; \varepsilon = \frac{1}{\text{Ec}\,\text{Pr}} \left| \frac{T_w}{T_r} - 1 \right|, \; \text{Ec} = \frac{(\gamma - 1) M^2}{\left| T_w / T_r - 1 \right|}.$$

Here N_δ, ε are the reference values, while $p, T, \mathbf{\Pi}, \mathbf{Q}$ are local cell values. Note that the degree of thermal nonequilibrium in macroscopic thermodynamic space is best represented by the composite number N_δ, not the Knudsen number alone, since the viscous force is a direct consequence of the thermal nonequilibrium effect [2]. In Fig. 25, it can be found that (1) there exist two distinctive regions of deceleration and acceleration (or gaseous compression and expansion) in the frontal and rear parts of the cylinder, respectively; (2) the degree of thermal nonequilibrium is high at the bow shock structure and at the rear part of cylinder where the strong expansion produces the most visible nonequilibrium as high as $\hat{R} = 17$; and (3) the NSF model in general over-estimates the degree of nonequilibrium, which can be considered the ultimate reason

behind its poor performance in high Knudsen and Mach number flows.

The last point may be further analyzed by recalling the non-Newtonian constitutive relation of the NCCR model [2], which is reproduced in Fig. 26. It is obvious that the constitutive relation is generally nonlinear and asymmetric, in particular, away from thermal equilibrium. Since gas particles experience deceleration (gas compression) at the bow shock structure, the normal stress in streamline direction, through $\Pi_{NSF}/p=(-)\mu u_x/p$, remains positive, meaning that the gas flow in that region is governed by the positive branch of NCCR in Fig. 26. In particular, the relatively larger shock structure thickness of the NCCR model observed in Figs. 22 and 25 (a) is due to the nonlinearity present in this positive branch of NCCR. Similarly, since gas particles experience rapid acceleration (severe expansion) at the rear part of the cylinder, the normal stress in streamline direction has negative sign, indicating that the gas flow in that region is governed by the negative branch of NCCR in Fig. 26. According to this explanation, relatively weaker gas expansion of the NCCR model (equivalently relatively stronger gas expansion of the NSF model) observed in Figs. 22 and 25 (a) is due to the smaller values of stress determined by the negative branch of NCCR. In summary, the ultimate origin of improved solutions of the NCCR model over the NSF model can be explained in concise manner by examining the degree of thermal nonequilibrium and the non-Newtonian nonlinear coupled constitutive relations.

5 Concluding remarks

An explicit modal DG scheme on triangular meshes has been developed for simulating all flow regimes of hypersonic rarefied and low speed microscale gases with a single framework. The new mixed DG scheme, which is based on the idea of adding auxiliary unknowns of high order non-conserved variables (stresses and heat fluxes), was developed for the spatial discretization of the conservation laws with complex non-Newtonian implicit NCCR models arising from the high degree of thermal nonequilibrium. The scheme retains all the advantages of

the original DG method including the generality of methodology for structured, unstructured, hybrid meshes with large complex grids.

The verification of the DG scheme was achieved by comparing numerical solutions of the NSF equation with the recently derived analytical counterpart for a stiff problem of the shock structure for all Mach numbers. In addition, the DG scheme on unstructured triangular meshes is validated by investigating the 2D hypersonic rarefied and low-speed microscale gas flows past a circular cylinder. It turned out that the DG results of the non-Newtonian NCCR model, while working for all Mach numbers, gave better agreement with experimental or DSMC data than the Newtonian linear NSF results in all cases of the problem studied.

In the conservation laws with the non-Newtonian NCCR, the viscous terms of diffusive nature play an even more important role in the numerical solutions than the Newtonian linear NSF equations. In the present study, the numerical treatment of viscous terms developed by Bassi and Rebey [8] was used for its simplicity and significance in the DG development. However, there have been other developments such as the method proposed by Cockburn and Shu [9]. Applications of these methods to the rarefied and microscale gas flow will be the next topic of the present line of research.

Acknowledgements

This work was supported by the National Research Foundation of Korea funded by the Ministry of Education, Science and Technology (Priority Research Centers Program NRF 2012-048078 and Basic Science Research Program 2012- R1A2A2A02-046270), South Korea. The authors gratefully acknowledge the substantial contributions of A. Karchani for producing the DSMC results using the sophisticated Bird’s code. The authors also thank the referees of this paper for their valuable and very helpful comments.

References

[1] J.M. Reese, M.A. Gallis, D.A. Lockerby, New directions in fluid dynamics: non-equilibrium aerodynamic and microsystem flows, Phil. Trans. Roy. Soc. Lond. A 361 (2003) 2967-2988.

[2] R.S. Myong, Thermodynamically consistent hydrodynamic computational models for high-Knudsen-number gas flows, Phys. Fluids. 11 (1999) 2788-2802.

[3] R.S. Myong, A generalized hydrodynamic computational model for rarefied and microscale diatomic gas flows, J. Comput. Phys. 195 (2004) 655-676.

[4] J.W. Ahn, C. Kim, An axisymmetric computational model for generalized hydrodynamic theory of rarefied and multi-species gas flows, J. Comput. Phys. 228 (2009) 4088-4117.

[5] R.S. Myong, A computational method for Eu's generalized hydrodynamic equations of rarefied and microscale gasdynamics, J. Comput. Phys. 168 (2001) 47-72.

[6] R.S. Myong, Impact of computational physics on multi-scale CFD and related numerical algorithms, Comput. Fluids. 45 (2011) 64-69.

[7] B.C. Eu, Kinetic Theory and Irreversible Thermodynamics, Wiley, 1992.

[8] F. Bassi, S. Rebay, A high-order accurate discontinuous finite element method for the numerical solution of the compressible Navier-Stokes equations, J. Comput. Phys. 131 (1997) 267-279.

[9] B. Cockburn, C.W. Shu, Runge-Kutta discontinuous Galerkin methods for convection dominated problems, J. Sci. Comput. 16 (2001) 173-261.

[10] L. Krivodonova, J. Xin, J.F. Remacle, N. Chevaugeonz, J.E. Flaherty, Shock detection

and limiting with discontinuous Galerkin methods for hyperbolic conservation laws, App. Numer. Math. 48 (2004) 323-338.

[11] H. Luo, J.D. Baum, R. Lohner, A discontinuous Galerkin method based on a Taylor basis for the compressible flows on arbitrary grids, J. Comput. Phys. 227 (2008) 8875-8893.

[12] H. Liu, K. Xu, A Runge-Kutta discontinuous Galerkin method for viscous flow equations, J. Comput. Phys. 224 (2007) 1223-1242.

[13] K. Kontzialis, J.A. Ekaterinaris, High order discontinuous Galerkin discretizations with a new limiting approach and positivity preservation for strong moving shocks, Comput. Fluids. 71 (2013) 98-112.

[14] B.Q. Li, Discontinuous Finite Elements in Fluid Dynamics and Heat Transfer, Springer, 2006.

[15] J. Iannelli, An implicit Galerkin finite element Runge-Kutta algorithm for shock structure investigations, J. Comput. Phys. 230 (2011) 260-286.

[16] J.S. Hesthaven, T. Warburton, Nodal Discontinuous Galerkin Methods, Springer, 2008.

[17] F.X. Gilardo, High-order triangle-based discontinuous Galerkin methods for hyperbolic equations on a rotating sphere, J. Comput. Phys. 214 (2006) 447-465.

[18] F.X. Gilardo FX, T. Warburton, A high-order triangular discontinuous Galerkin oceanic shallow water model, Int. J. Numer. Meth. Fluids. 56 (2008) 899-925.

[19] H. Luo, K. Xu, A discontinuous Galerkin method based on a gas kinetic scheme for the Navier-Stokes equations on arbitrary grids, Computational Fluid Dynamics (2009) 423-428.

[20] M. Raalte, B. van Leer, Bilinear forms for the recovery-based discontinuous Galerkin method for diffusion, Comm. Comput. Phys. 5 (2009) 683-693.

[21] F.P.T Baaijens, Mixed finite element methods for viscoelastic flow analysis: a review, J. Non-Newtonian Fluid Mech. 79 (1998) 361-385.

[22] M. Linzer, D.F. Hornig, Structure of shock fronts in argon and nitrogen, Phys. Fluids 6 (1963) 1661-1668.

[23] B. Schmidt, Electron beam density measurements in shock waves in argon, J. Fluid Mech. 39 (1969) 361-373.

[24] H. Alsmeyer, Density profiles in argon and nitrogen shock waves measured by the absorption of an electron beam, J. Fluid Mech. 74 (1976) 497-513.

[25] J.M. Reese, L.C. Woods, F.J. Thivet, S.M. Candel, A second-order description of shock structure, J. Comput. Phys. 117 (1995) 240-250.

[26] K. Morinishi, Numerical simulation for gas microflows using Boltzmann, Comput. Fluids, 35 (2006) 978-985.

[27] J.Y. Yang, J.C. Huang, Rarefied flow computations using nonlinear model Boltzmann equations, J. Comput. Phys. 120 (1995) 323-339.

[28] F.W. Vogenitz, G.A. Bird, J.E. Broadwell, H. Rungaldier, Theoretical and experimental study of rarefied supersonic flows about several simple shapes, AIAA J. 6 (1968) 2388-2394.

[29] W. Wetzel, H. Oertel, Direct Monte Carlo simulations of hypersonic flows past blunt bodies, Progr. Astronaut. Aeronaut. 118 (1989) 432-446.

[30] M. Fossati, A. Guardone, L. Vigevano, K. Xu, Kinetic node-pair formulation for two-dimensional flows from continuum to transitional regime, AIAA J. 51-4 (2013) 784-796.

[31] X. Zhang, C. W. Shu, On positivity-preserving high order discontinuous Galerkin schemes for compressible Euler equations on rectangular meshes, J. Comput. Phys. 229 (2010) 8918-8934.

[32] L. Krivodonova, Limiters for high-order discontinuous Galerkin methods, J. Comput. Phys. 226 (2007) 879-896.

[33] R.S. Myong, Gaseous slip model based on the Langmuir adsorption isotherm, Phys. Fluids 16 (2004) 104-117.

[34] N.T.P Le, C. White, J.M. Reese, R.S. Myong, Langmuir-Maxwell and Langmuir-Smoluchowski boundary conditions for thermal gas flow simulations in hypersonic aerodynamics, Int. J. Heat Mass Trans. 55 (2012) 4929-5378.

[35] J.A. Trangenstein, Numerical Solution of Hyperbolic Partial Differential Equations, Cambridge University Press, 2007.

[36] W.J. Rider, R.B. Lowrie, The use of classical Lax-Friedrichs Riemann solvers with discontinuous Glaerkin method, Int. J. Numer. Meth. Fluids 40 (2002) 479-486.

[37] K.A. Hoffmann, Computational Fluid Dynamics, Engineering Education System, 1989.

[38] G.E. Karniadakis, S.J. Sherwin, Spectral/hp Element Methods for CFD, Oxford University Press, 1999.

[39] M. Dubiner, Spectral methods on triangles and other domains, J. Sci. Comput. 6 (1991) 345-390.

[40] E. Hopf, The partial differential equation $u_t + uu_x = \mu u_{xx}$, Comm. Pure. Appl. Math. 3 (1950) 201-230.

[41] I.V. Karlin, G. Dukek, T.F. Nonnenmacher, Invariance principle for extension of hydrodynamics: nonlinear viscosity, Phys. Rev. E 55-2 (1997) 1573-1576.

[42] D. Jou, J. Casas-Vazquez, G. Lebon, Extended Irreversible Thermodynamics, Springer, New York, 2006.

[43] S. Chapman, T.G. Cowling, The Mathematical Theory of Non-Uniform Gases, Third Edition, Cambridge University Press, 1970.

[44] H. Grad, The profile of a steady plane shock wave, Comm. Pure. Appl. Math. 5 (1952) 257-300.

[45] R.S. Myong, Analytical solutions of shock structure thickness and asymmetry within Navier-Stokes/Fourier framework, AIAA J. (2014) DOI: 10.2514/1.J052583., http://acml.gnu.ac.kr (11/2013).

[46] F.E. Lumpkin, D.R. Chapman, Accuracy of the Burnett equations for hypersonic real gas flows, J. Thermo. Heat Trans. 3 (1992) 419-425.

[47] G.A. Bird, http://www.gab.com.au (05/2013).

Figures

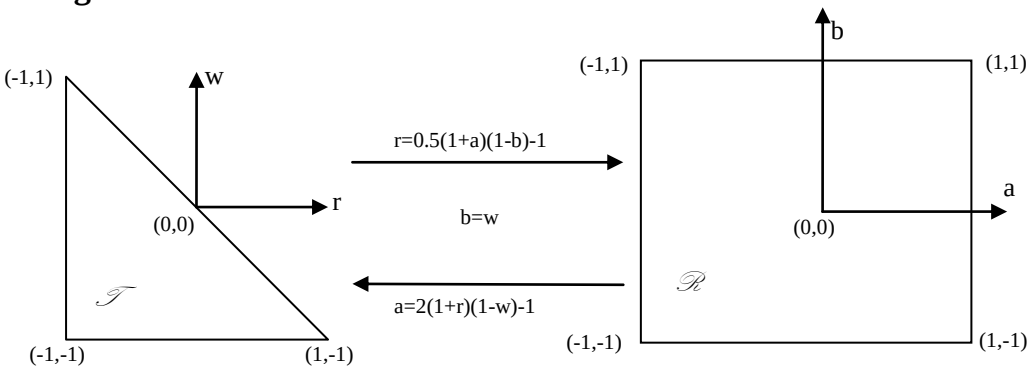

Fig. 1. Reference element for defining the basis function.

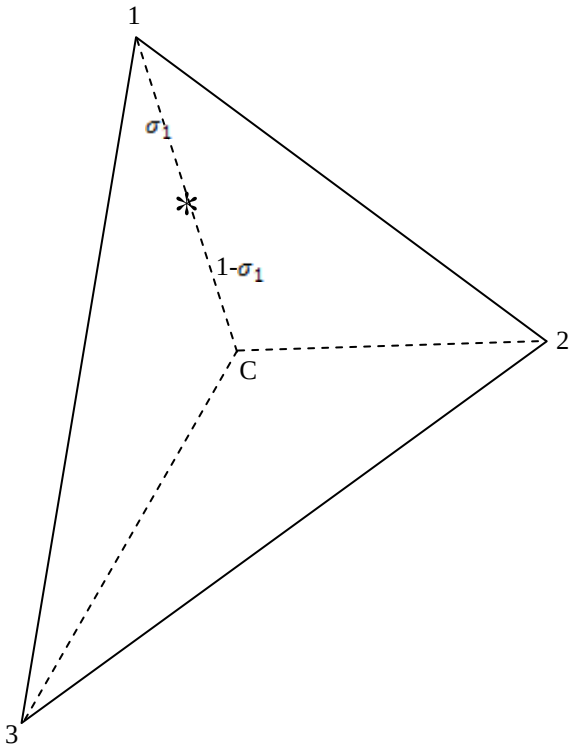

Fig. 2. New scheme of positivity preserving limiter for triangular element.

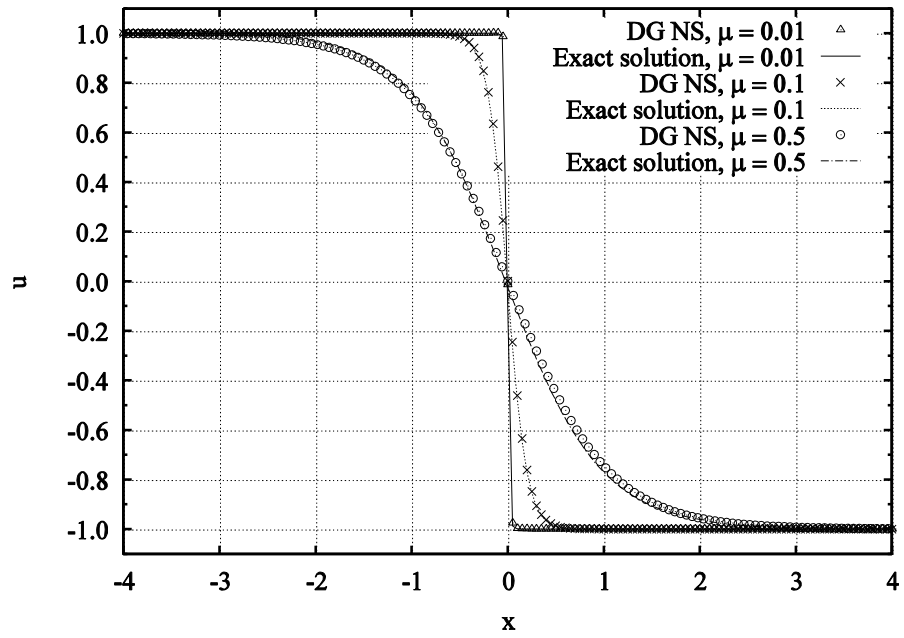

Fig. 3. Computed shock structure profiles for the linear 1D Burgers equation at various values of the viscosity μ.

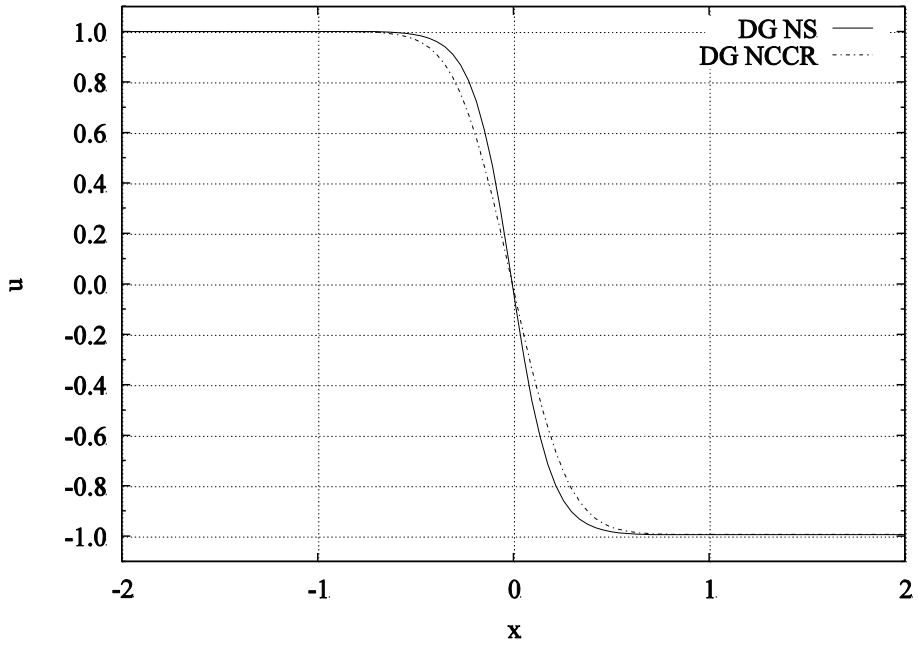

Fig. 4. Comparison of the numerical solutions of the linear 1D Burgers and 1D NCCR-Burgers equations for a viscosity value $\mu = 0.1$.

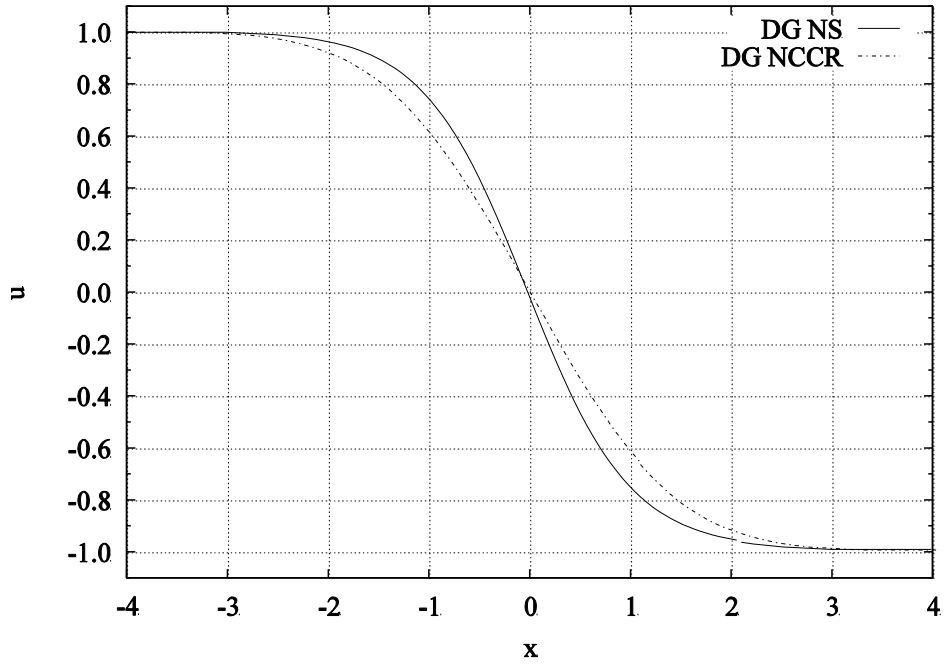

Fig. 5. Comparison of the numerical solutions of the linear 1D Burgers and 1D NCCR-Burgers equations for a viscosity value $\mu = 0.5$.

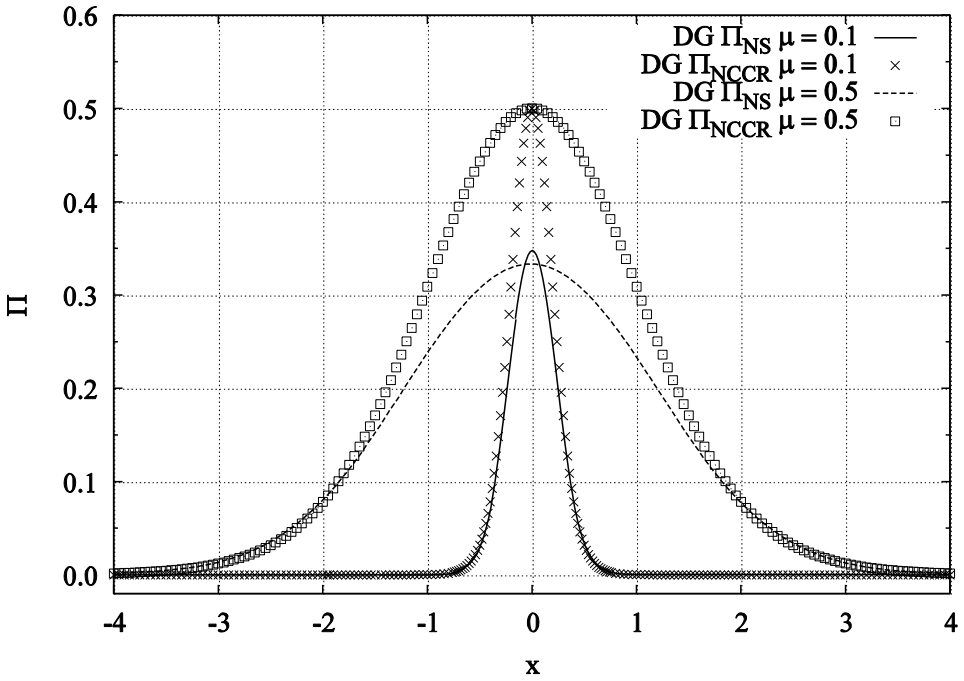

Fig. 6. Numerical solutions of the stress Π for the linear 1D Burgers and 1D NCCR-Burgers equations.

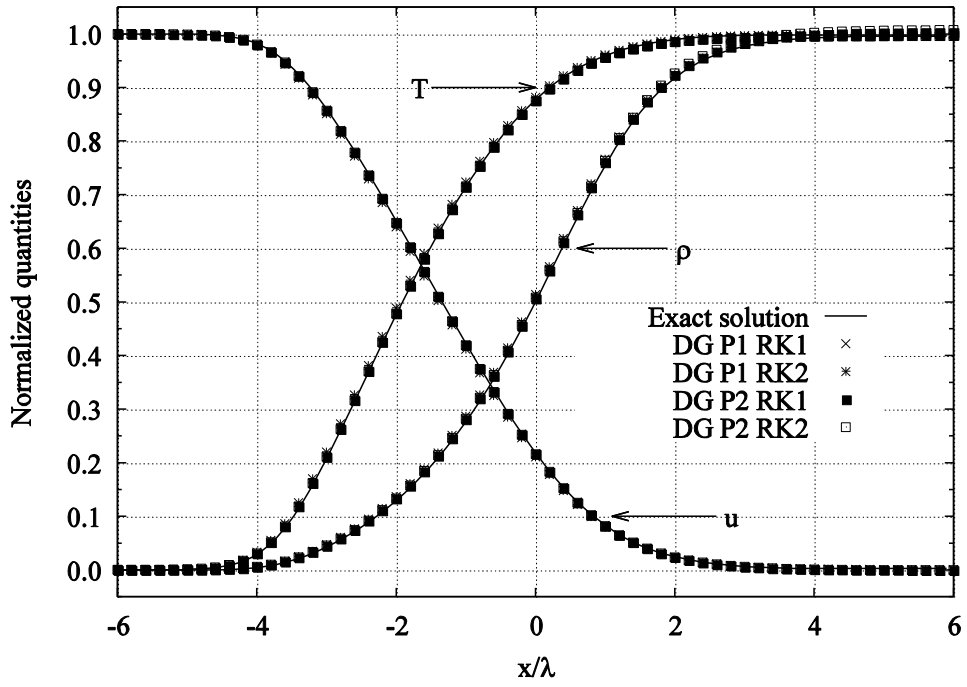

Fig. 7. Computed shock structure profiles of the NSF model for different types of elements and the Runge-Kutta time-marching methods (M = 5).

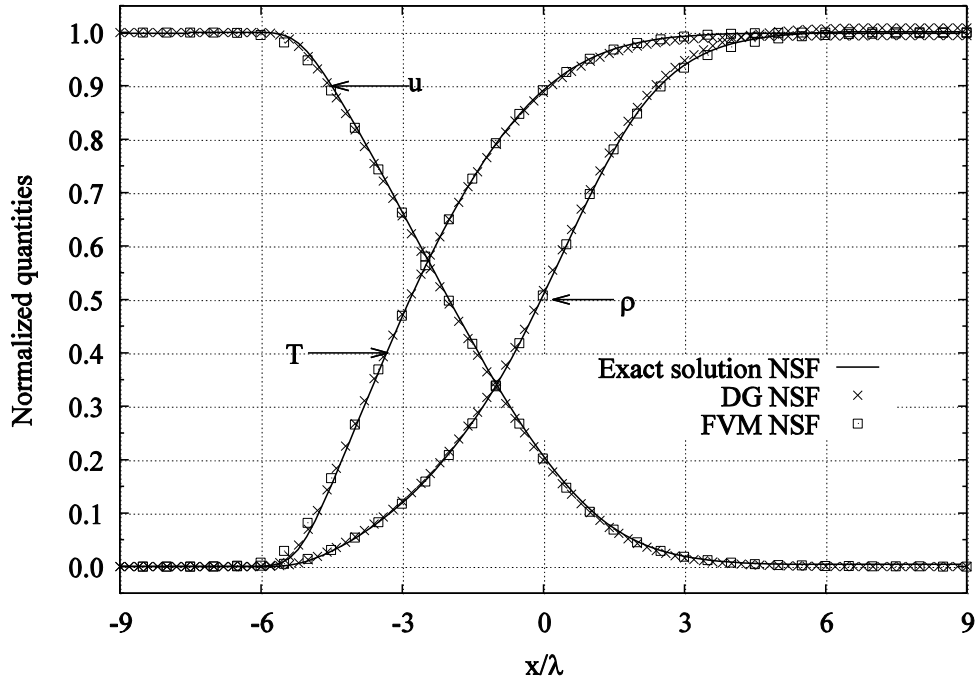

Fig. 8. Comparison of the numerical solutions of the 1D DG and 1D FVM schemes for the NSF model (M = 8).

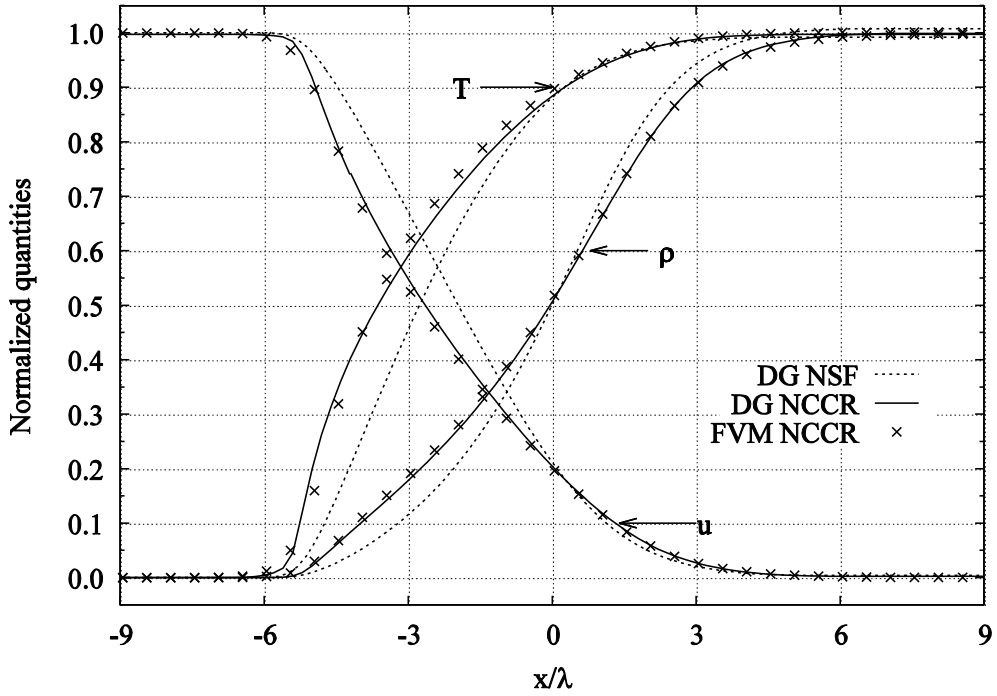

Fig. 9. Computed shock structure profiles of the NSF (DG) and NCCR (DG, FVM) models (M = 8).

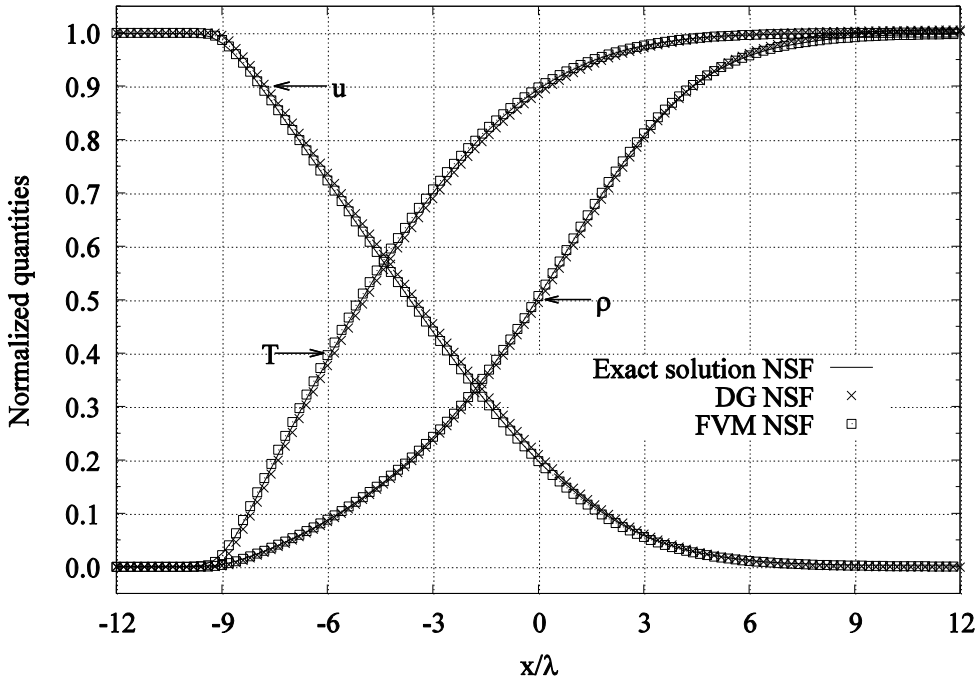

Fig. 10. Comparison of the numerical solutions of the 1D DG and 1D FVM schemes for the NSF model (M = 15).

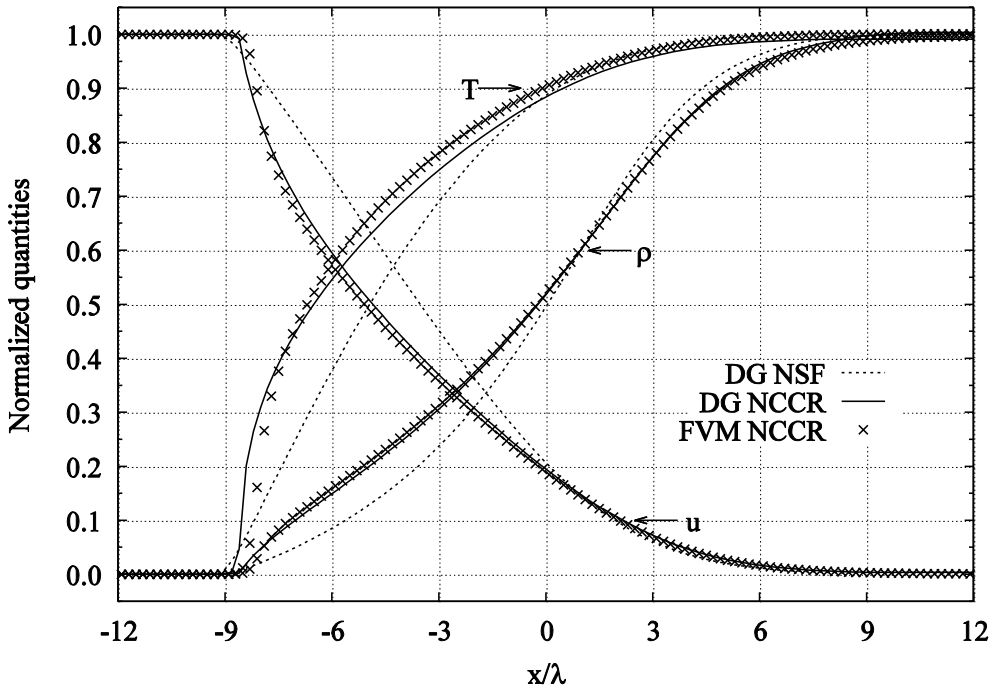

Fig. 11. Computed shock structure profiles of the NSF (DG) and NCCR (DG, FVM) models (M = 15).

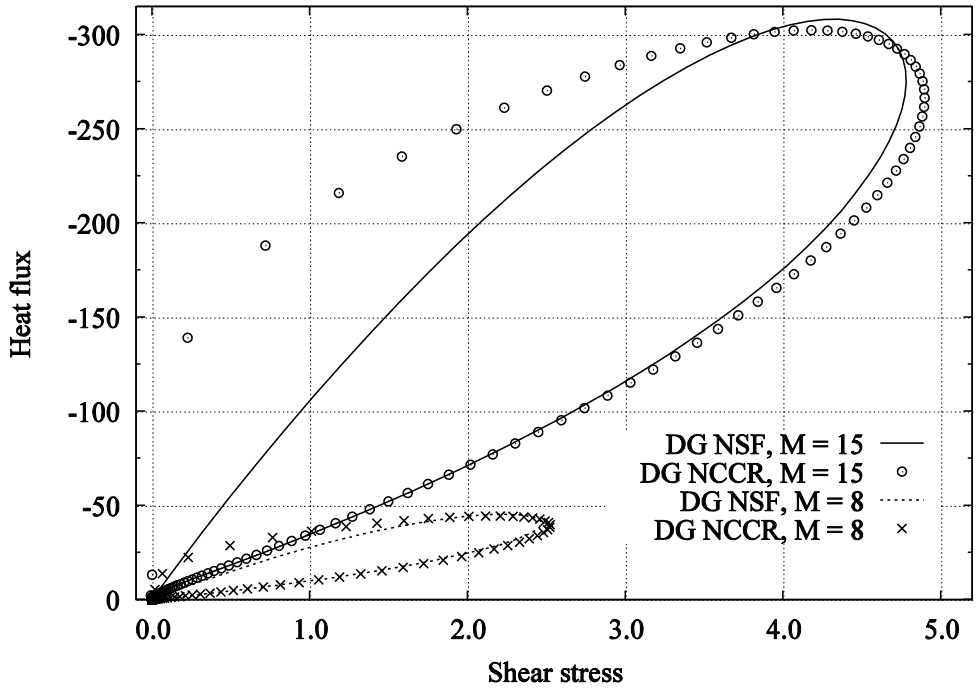

Fig. 12. Computed heat flux and shear stress of the NSF and NCCR models (M = 8, 15).

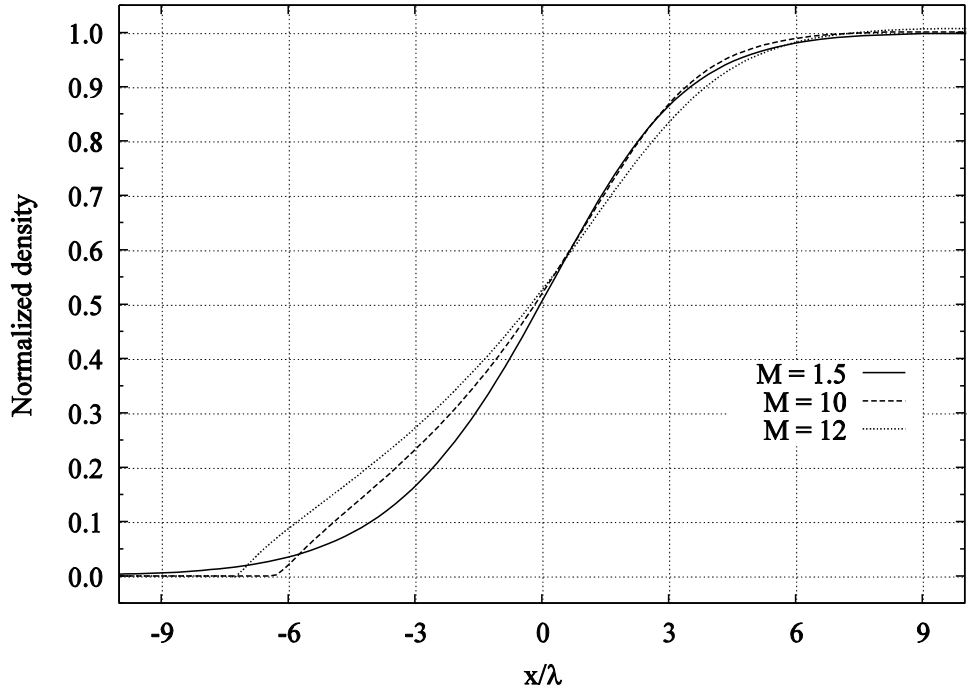

Fig. 13. Normalized density profiles at various Mach numbers for the NCCR model.

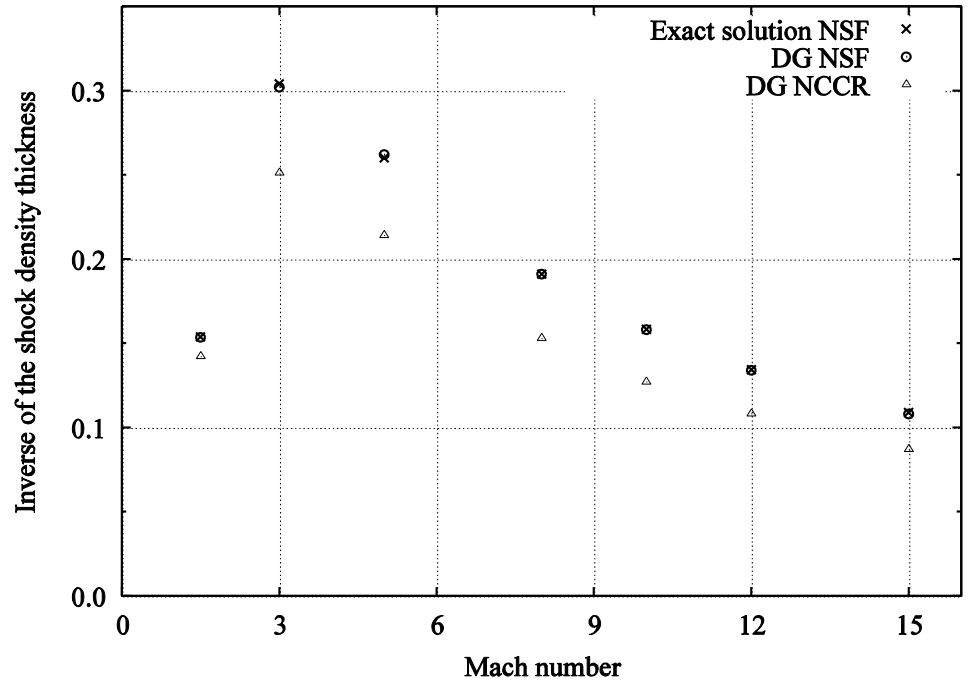

Fig. 14. Comparison of the inverse shock density thickness for the DG NSF and NCCR models and experimental data (Maxwellian gas, s = 1.0, c = 1.0138, Pr = 0.75).

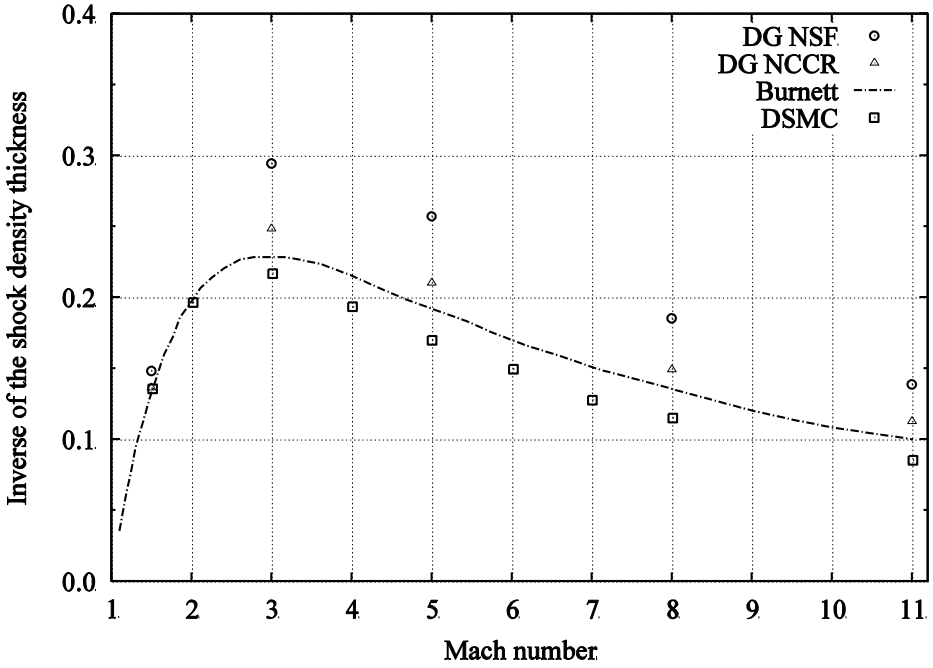

Fig. 15. Comparison of the inverse shock density thickness for the DG NSF and NCCR models and the Burnett and DSMC data [42] (Maxwellian gas, s = 1.0, c = 1.0138, Pr = 2/3).

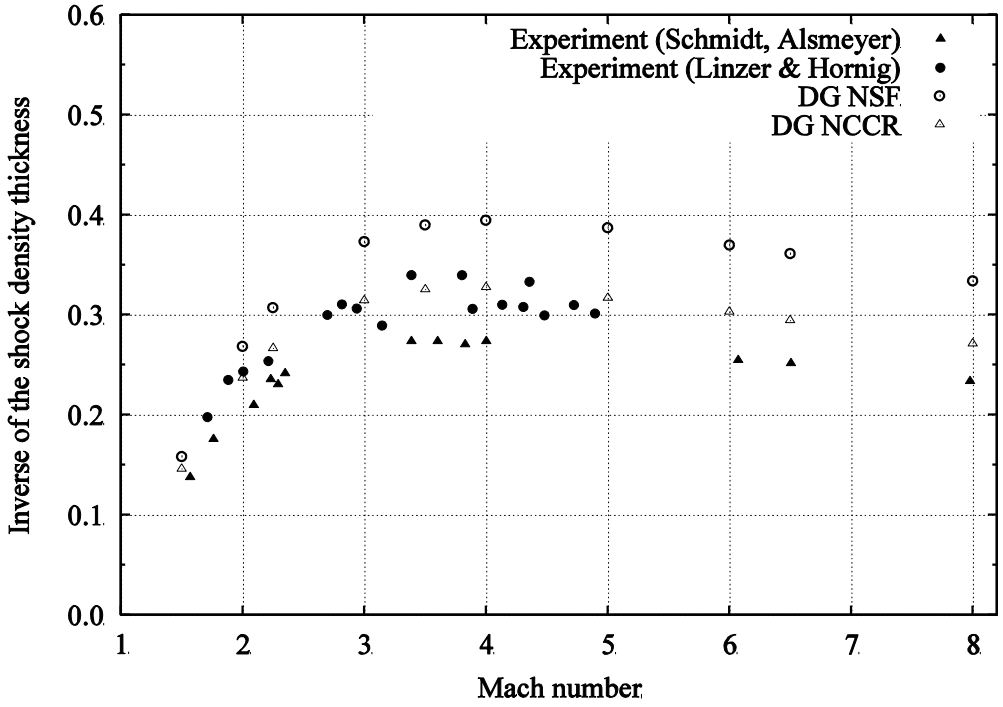

Fig. 16. Comparison of the inverse shock density thickness for the DG NSF and NCCR models and experimental data [21-23] (argon gas, s = 0.8, c = 1.0179, Pr = 2/3).

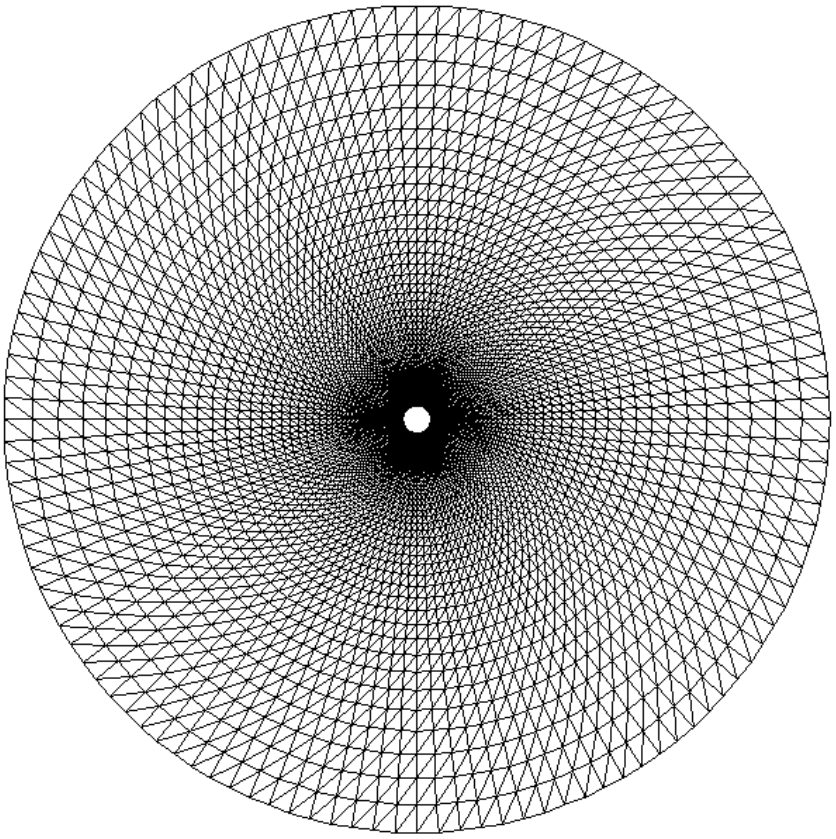

Fig. 17. An example of unstructured triangular meshes for the cylinder case.

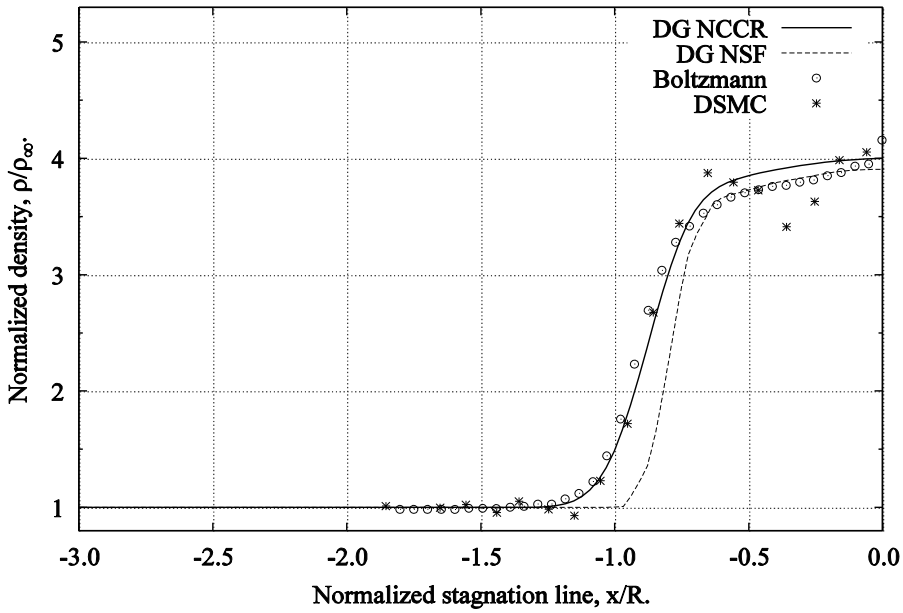

Fig. 18. Normalized density distribution along the normalized stagnation line of the hypersonic case, M = 5.48 and Kn = 0.05.

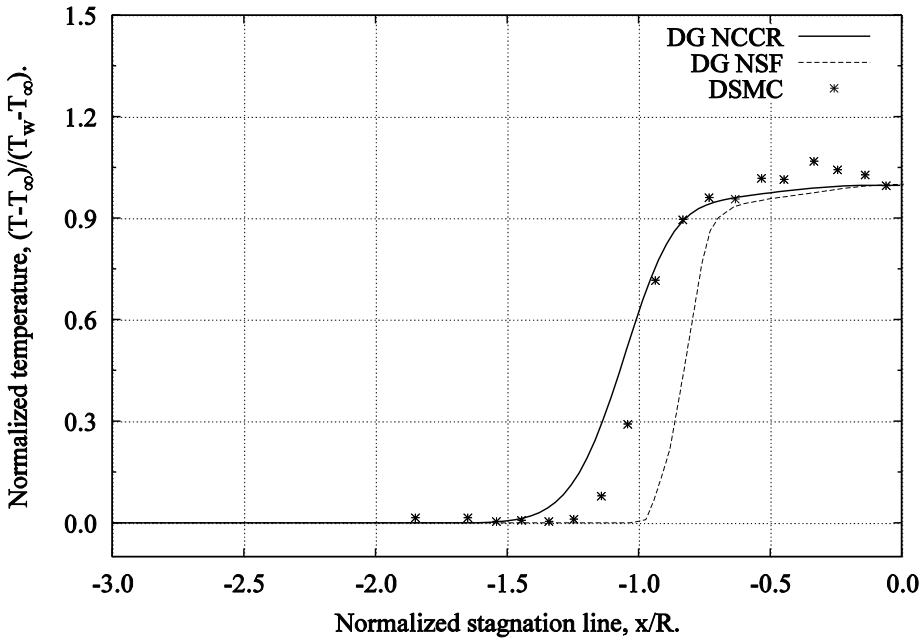

Fig. 19. Normalized temperature distribution along the normalized stagnation line of the hypersonic case, M = 5.48 and Kn = 0.05.

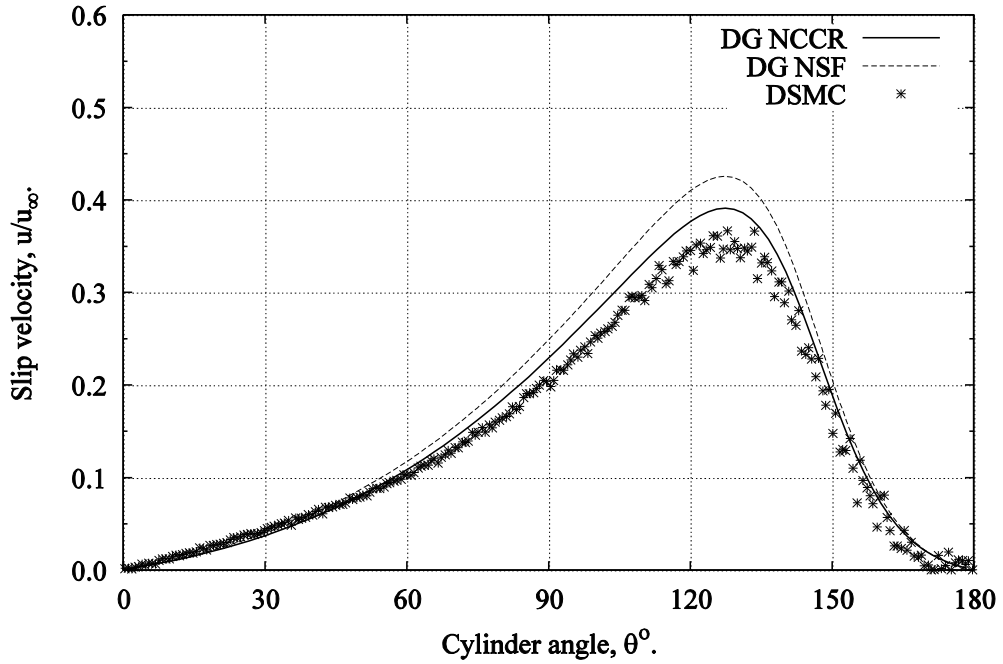

Fig. 20. Normalized slip velocity around the cylinder surface of the hypersonics case, M = 5.48 and Kn = 0.05.

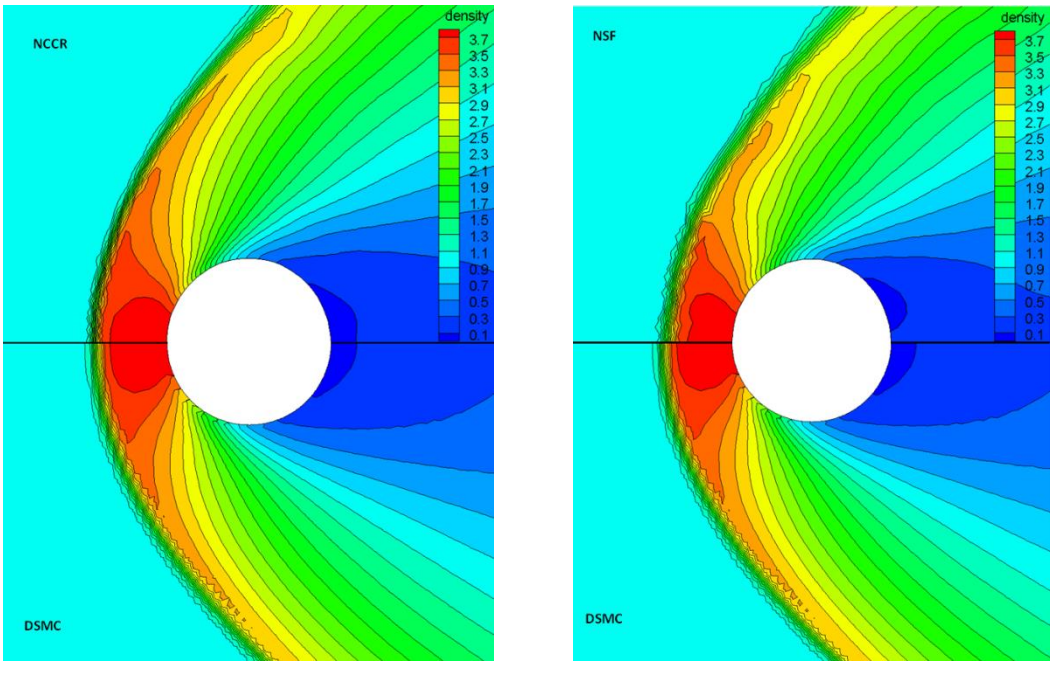

a) b)

Fig. 21. Normalized density (ρ/ρ_∞) fields and contours of the hypersonic case, M = 5.48 and Kn = 0.05: a) NCCR and DSMC, and b) NSF and DSMC.

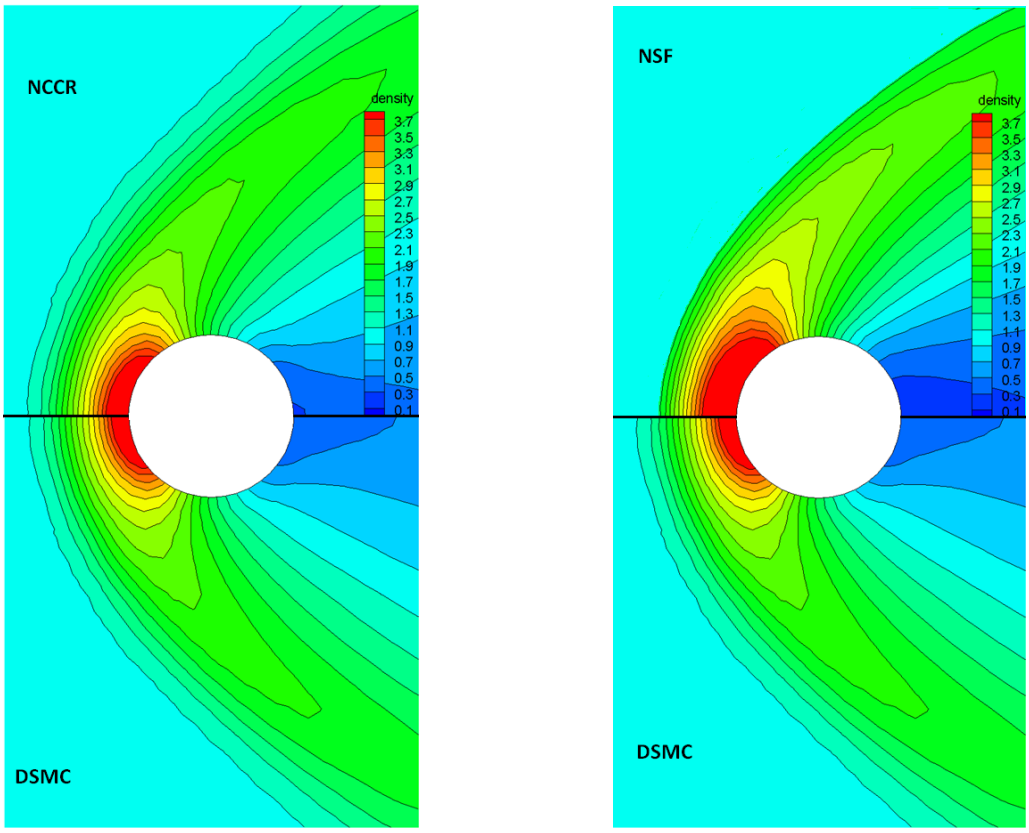

a) b)

Fig. 22. Normalized density (ρ/ρ_∞) fields and contours of the hypersonic case, M = 5.48 and Kn = 0.5: a) NCCR and DSMC, and b) NSF and DSMC.

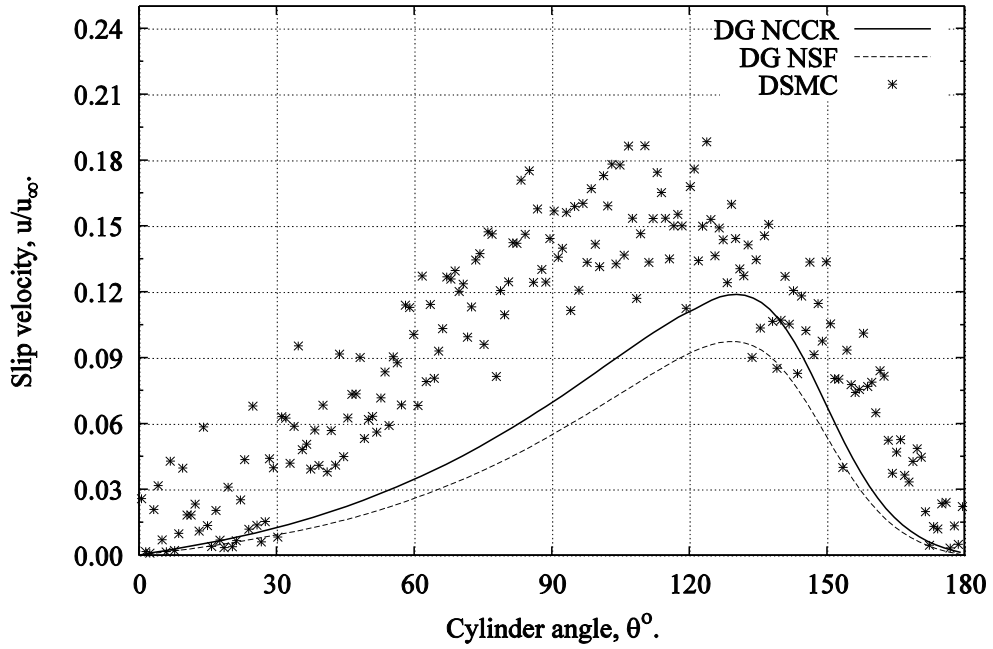

Fig. 23. Normalized slip velocity around the cylinder surface of the microscale case, M = 0.1 and Kn = 0.1.

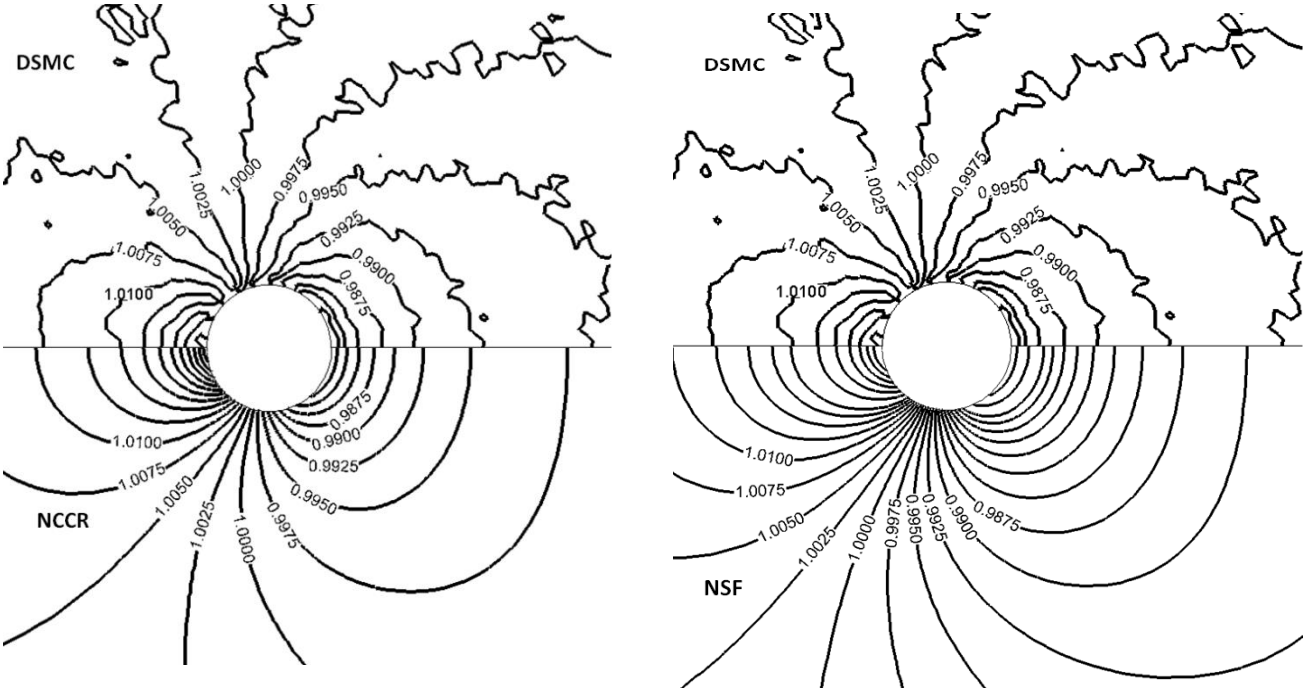

a) b)

Fig. 24. Normalized density (ρ/ρ_∞) contours of the microscale case, M = 0.1 and Kn = 0.1: a) DSMC and NCCR and b) DSMC and NSF.

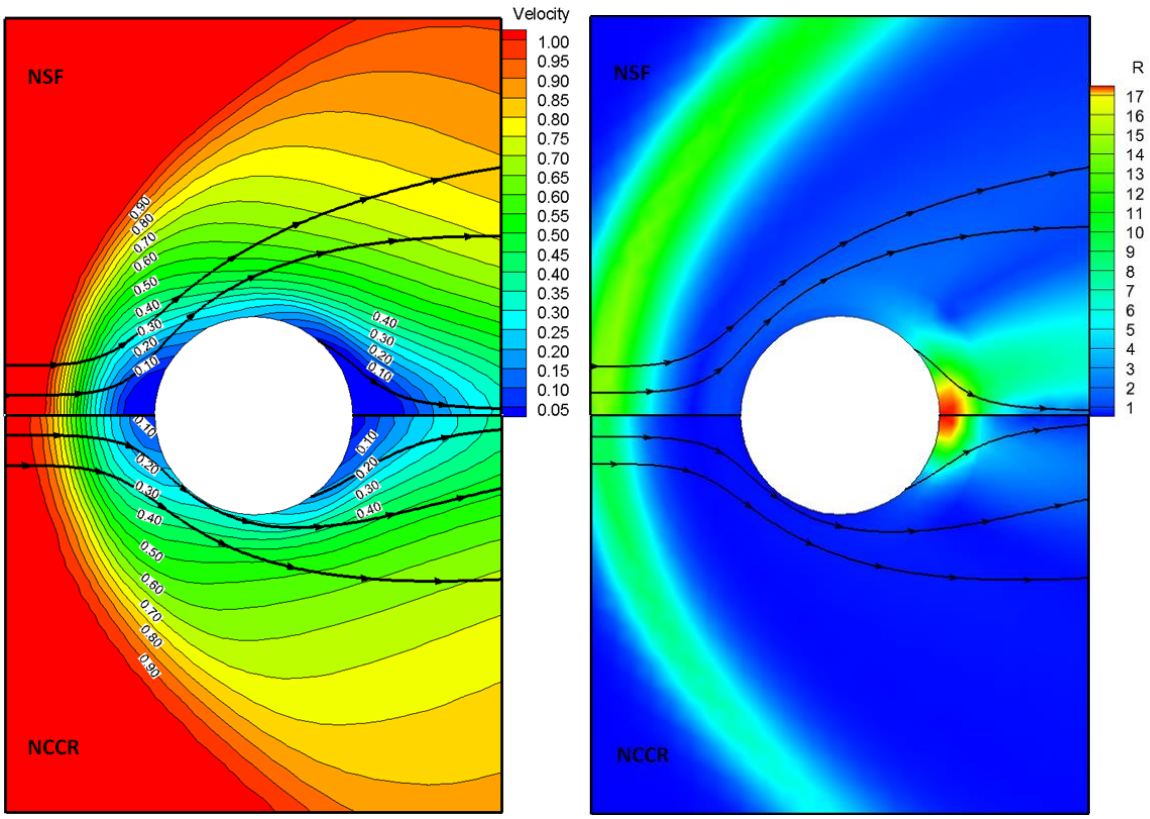

a) b)

Fig. 25. Contours of scalar values and streamlines, M = 5.48 and Kn = 0.5: a) velocity magnitude and b) degree of non-equilibrium $\hat{R}$.

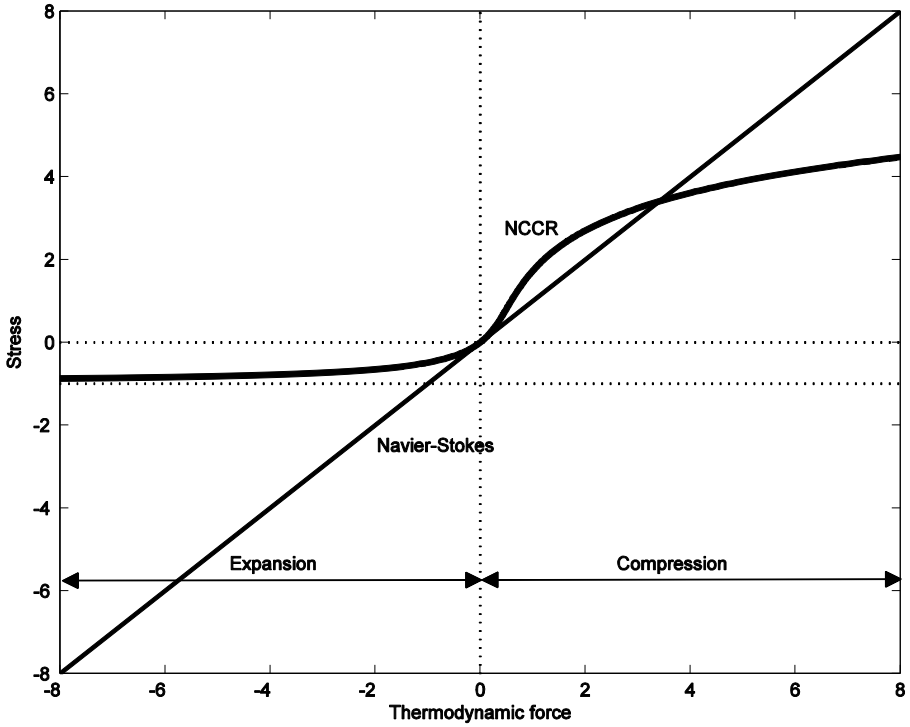

Fig. 26. Constitutive relations in compression and expansion flows. The horizontal axis represents the thermodynamic force by velocity gradient $\hat{\Pi}_0$, while the vertical axis represents the normal stress $\hat{\Pi}$.